Development of a novel test method to investigate mode II fracture and dissection of arteries

Brian FitzGibbon, Patrick McGarry*
Biomedical Engineering, National University of Ireland Galway, Galway, Ireland
*Corresponding author: patrick.mcgarry@nuigalway.ie

Abstract

The current study presents the development and implementation of a novel experimental technique to generate and characterise mode II crack initiation and propagation in arterial tissue. The current study begins with a demonstration that lap-shear testing of arterial tissue results in mixed mode fracture, rather than mode II. We perform a detailed computational design of a novel experimental method (which we refer to as a shear fracture ring test (SFRT)) to robustly and repeatably generate mode II crack initiation and propagation in arteries. This method is based on generating a localised region of high shear adjacent to a cylindrical loading bar. Placement of a radial notch in this region of high shear stress is predicted to result in a kinking of the crack during a mode II initiation and propagation of the crack over a long distance in the *c*-direction along the *c*-*a* plane. Fabrication and experimental implementation of the SFRT on excised ovine aorta specimens confirms that the novel test method results in pure mode II initiation and propagation. We demonstrate that the mode II fracture strength along the *c*-*a* plane is eight times higher than the corresponding mode I strength determined from a standard peel test. We also calibrate the mode II fracture energy based on our measurement of crack propagation rates. The mechanisms of fracture uncovered in the current study, along with our quantification of mode II fracture properties have significant implications for current understanding of the biomechanical conditions underlying aortic dissection.

Keywords: Soft tissue fracture; Arterial dissection; Soft tissue anisotropy; Finite element; Experimental fracture mechanics.

1 Introduction

Aortic dissection is a lethal disease which can lead to stroke, spinal cord infarction, renal failure, cardiac tamponade, aortic rupture, and death [1–3]. Mortality rates can be as high as 1% per hour [1,4]. However, to date the exact pathophysiological processes and related biomechanisms underlying aortic dissection have not been uncovered. Previous investigations of the damage and fracture properties of arterial tissue have primarily relied on peel tests [5–9]. Such a test methodology results in a mode I fracture and allows for the calibration of a mode I fracture strength (reported to be in the region of 140 kPa [7]). However, given the anisotropic mechanical behaviour of arterial due to its complex microstructure, which consists of families of aligned collagen and elastin fibres, the mode and mechanism of crack propagation induced by a standard peel test is of limited relevance to the physiological process of artery dissection and rupture. Given that the high blood pressure in the lumen is the primary source of loading of arterial tissue in vivo, we argue that aortic dissection results from mode II fracture initiation, rather than mode I. Lumen pressure loading induces a high compressive radial component of stress throughout the artery wall, such that a mode I initiation of a dissection in the orthogonal circumferential-axial plane (as observed clinically) is highly improbable. Iatrogenic dissections may follow from mixed mode fracture initiation [10], but such dissections primarily result from catheterisation, percutaneous transluminal coronary angioplasty, or cardiac surgery [11]. In any event, iatrogenic dissections are reported to occur in the radial-axial plane [12], which, given the highly anisotropic arterial microstructure, is not at all reflective of the mode I fracture in the circumferential-axial plane induced by a standard peel test. Every aortic dissection involves circumferential and axial crack propagation, whereas not all are associated with a radial crack propagation [1,11,13]. A recent experimental study qualitatively observed a similar trend of dissection in the circumferential-axial plane of excised aortas subjected to hypertensive levels of lumen fluid pressure [14]. Such dissection propagation in the circumferential-axial plane is also reported for canine thoracic aortas, where it is qualitatively suggested that bond strength between lamellae are weaker than the lamellae material strength [15].

To gain further insight into the clinical observation of arterial dissection in the circumferential-axial plane it is essential to accurately characterise the fracture properties of arterial tissue under such mode II loading conditions. Classical mode II lap-shear fracture mechanics experiments have been carried out by Witzenburg et al. [16] on porcine ascending aorta and by Sommer et al. [17] on excised human aneurysmatic and dissected aorta. However, we present a preliminary finite element analysis of lap-shear testing of arterial tissue in Section 1.1 (below) in which we demonstrate that the high levels of material deformation at the point of fracture initiation consequently results in a mixed mode initiation and propagation, rather than the intended mode II fracture. The generation of a mode II crack in highly deformable, high toughness fibrous soft tissue under controlled experimental conditions remains a significant challenge. This challenge cannot be addressed by standard test

methodologies developed for traditional engineering materials, such as lap shear tests. A further challenge is that fracture testing of naturally occurring biological materials such as arteries does not facilitate the engineering of standardised fracture specimen geometries. Therefore, implementation and interpretation of fracture testing subject to the limitation of non-standard geometries, such as arteries, requires in-depth mechanistic analysis.

In the current study we design, develop, and validate a novel test methodology for the initiation and propagation of mode II dissection in arterial tissue in the circumferential-axial plane. We demonstrate that this pattern of mode II dissection is highly repeatable. Such mode II fracture always preferentially occurs in our experiments, in contrast to mode I fracture in the radial-axial plane, which never occurs due to the significant toughening mechanism of collagen alignment at the crack-tip. Using our novel experimental methodology, in parallel with cohesive zone modelling of our experiments, we determine the pure mode II fracture strength and fracture energy of ovine aortas. We demonstrate that the mode II fracture strength is approximately eight times higher than the mode I fracture strength measured using a traditional peel test. Finally, we discuss the implications of our results in terms of advancing the current understanding of the biomechanics of artery dissection.

1.1 Lap-shear testing of arterial tissue results in a mixed mode crack propagation

Due to the high strength and toughness of arterial tissue, significant material deformation occurs in lap-shear tests prior to damage initiation and crack propagation. This is clearly illustrated by the experiments of Sommer et al. [17] (referred to hereafter as *constrained lap-shear testing*) and Witzenburg et al. [16] (referred to hereafter as *unconstrained lap-shear testing*). In the *constrained lap-shear tests* the top and bottom surfaces of the artery sample are bonded to rigid horizontal plates. In the *unconstrained lap-shear tests* the top and bottom surfaces of the artery sample are unconstrained. In Figure 1 we present finite element cohesive zone analysis of the constrained experiments of Sommer et al. [17] and the unconstrained experiments of Witzenburg et al. [16] in which crack initiation and propagation is simulated using a cohesive zone formulation. The fracture strength is calibrated so that predicted crack initiation occurs at an identical level of applied shear deformation as reported experimentally. Mode mixity is defined as $\varphi_{MM} = \tan^{-1}(T_t/T_n)$ and is presented as a function of normalised crack tip position, where T_t and T_n are the tangential (shear) and normal tractions, respectively, at the crack-tip. Full details of the artery anisotropic hyperelastic material law are presented in Appendix A, and the calibration of the material law to arterial tissue is presented in Section 3.1. The cohesive zone fracture model developed in this study is presented in Appendix B and provides an advance on previous coupled mixed mode formulations by facilitating independent specification of mode-dependent fracture strength and fracture energy independent of intrinsic interface stiffness, while ensuring positive instantaneous incremental positive dissipation [18].

As shown in Figure 1(a), simulation of a *constrained lap-shear test*, predicts a mode mixity of ~0.2107 at fracture initiation, with a mean mode mixity of $\varphi_{MM} = \sim 0.1157$ rad (~6.63°) during subsequent crack propagation. Remarkably, this represents a mode mixity that is closer to mode I, rather than the intended mode II fracture. Figure 1(b) illustrates the high level of material deformation at the crack-tip throughout, resulting in a localised mode of loading that resembles a peel test rather than a mode II fracture test. Also shown in Figure 1, simulation of an *unconstrained lap-shear test* predicts a mode mixity of ~1.229 at fracture initiation, with a mean mode mixity of $\varphi_{MM} = \sim 1.236$ rad (~70.85°) during subsequent crack propagation. Again, this is quite different from the intended mode II fracture ($\varphi_{MM} = \pi/2$ rad). Figure 1(c) demonstrates the high levels of material deformation at initiation and during propagation, resulting in normal tractions at the crack-tip that are comparable in magnitude to corresponding tangential tractions.

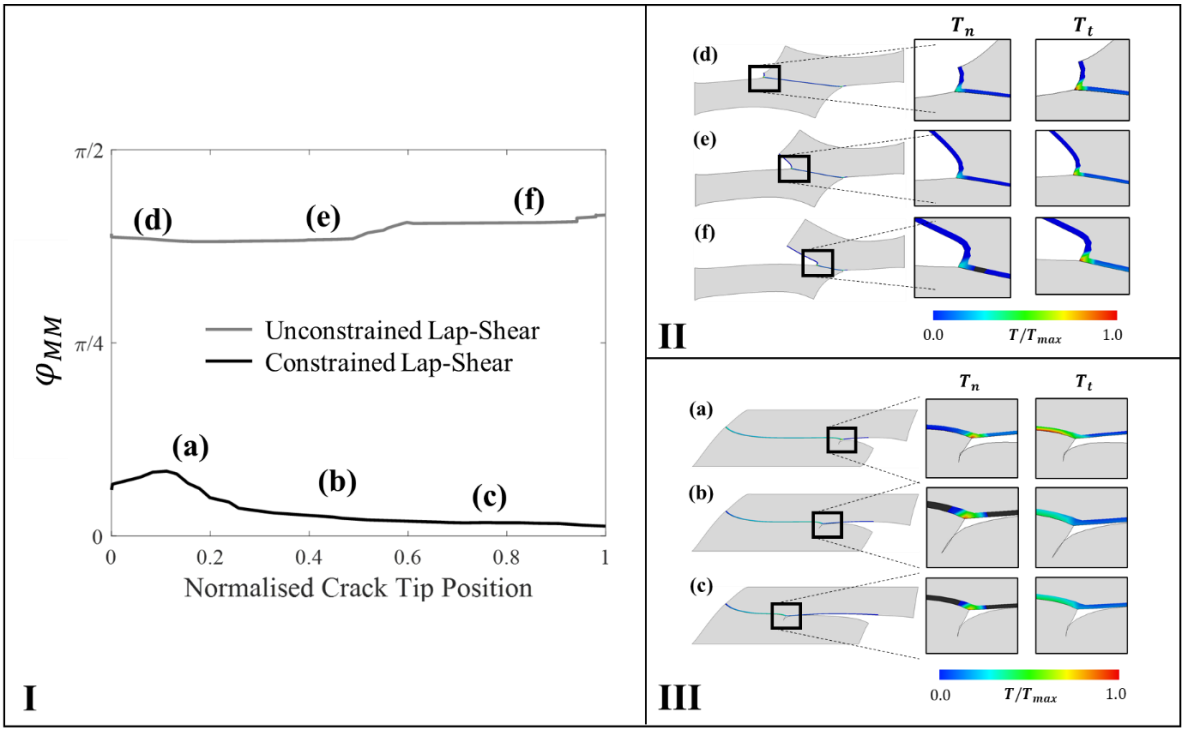

Figure 1. (I) Mode mixity (ϕ_{MM}) as a function of normalised crack tip position for a constrained in-plane lap shear test and an unconstrained lap-shear test; (II) Simulation of an unconstrained lap-shear test where normal and tangential traction is shown. Cohesive zone parameters used were ($\sigma_{max} = 200\ kPa, G_n^0 = 0.003\ N/mm, \tau_{max} = 400\ kPa, G_t^0 = 0.003\ N/mm$); (III) Simulation of a constrained lap-shear test. The traction at the crack tip is predominantly a mode I traction. Cohesive zone parameters used were ($\sigma_{max} = 200\ kPa, G_n^0 = 0.003\ N/mm, \tau_{max} = 400\ kPa, G_t^0 = 0.003\ N/mm$). Full details of the artery anisotropic hyperelastic material law and the cohesive zone fracture model are presented in Appendix A and Appendix B, respectively.

As neither unconstrained nor constrained lap-shear test protocols result in mode II fracture, in the current study we aim to develop a novel test methodology to induce pure mode II fracture initiation and crack propagation in arterial tissue. We argue that the quantitative analysis of pure mode II fracture resistance of arterial tissue is of critical importance. Lumen blood pressure is the primary source of mechanical loading on an artery wall in vivo, resulting in a compressive radial component of stress. Therefore, we suggest that mode I initiation of fracture is not possible under in vivo loading and that arterial dissection results from mode II fracture of arterial tissue.

2 Design and computational validation of a novel experimental mode II fracture test (shear fracture ring test (SFRT))

In this section we outline the analysis and design of a novel experimental methodology that results in pure mode II crack propagation in aortic tissue. Motivated by an analytical solution developed by Parry and McGarry [19] for the stress state of a bi-layered composite arch, we note that interface tractions vary from mode I at the top of the arch to mode II at the side of the arch. Attachment of a straight bi-layered composite strut to the bi-layered arch (representing a typical stent design) further increases the shear stress at the base of the arch [19]. Extending this analysis of the transition of interface from normal stress at the top of an arch to a shear stress at the side of the arch, we propose a test method in which a section ("ring") of excised artery is mounted on two cylindrical loading bars. The loading bars are then moved apart, imposing a deformation on the artery ring such that that two curved "arch-type" sections (top and bottom) are developed, connected by straight "strut-type" sections, as shown in Figure 2(a). This generates a localised region of high shear stress at the sides of the cylindrical loading bars (analogous to the maximum shear stress at the base of the stent arch uncovered in the study by McGarry and Parry [19]).

Computational design of experiment

A schematic of the computational design of experiment modelling procedure is outlined in Figure 2(a). A ring of excised aortic tissue with radius R_s is placed onto two steel bars of radius r_b. The bottom bar is fixed throughout the analysis while the top bar is displaced at a constant strain rate such that at any time point the distance travelled by the top bar is equal to u. We define a deformed interface coordinate S (shown in Figure 2(a)) which describes the position along a quarter circumference of the deformed configuration. S begins at the top of the bar and describes the position that is distance d through

the thickness t and ends at $S = L$. We also define a radial coordinate r_{ct} which describes the radial position of the crack tip through the wall. The original circumference of the ring is described as $C_0 = 2(L_0) + 2\pi(r_b + t/2)$ where L_0 is the distance from the midpoint of one loading bar to the other. The change in circumference is described as follows: $\Delta C = \Delta L$ where ΔL is the displacement applied to the upper loading bar. Also shown in Figure 2(a) is a local/material coordinate system for the artery ring; r, c, a indicating axes corresponding to the physiological radial, circumferential, axial axes, respectively. Collagen fibres are assumed to lie in the c-a plane [20,21]. A measure of nominal strain in the *c*-direction (the physiological circumferential direction) is then given as the $E_{cc} = \Delta C/C_0$ where C_0 is the undeformed circumference of the ring. Hereafter, for brevity, E_{cc} is referred to as the nominal *circumferential strain* imposed on the artery ring. The novel test methodology is referred to as the *SFRT* hereafter.

A finite element analysis of the *SFRT* is presented in Figure 2(b). Figure 2(b) shows a contour plot of circumferential stress σ_{cc} (normalised by the initial shear modulus μ) for the case of a loading bar of radius $r_b/R_s = 0.18$. The circumferential stress is the dominant stress component in the artery ring; it is five times higher than the corresponding peak maximum shear stress τ (when $r_b/R_s = 0.18$) which occurs at the side of the arch region, as shown in Figure 2(c). The magnitude of τ at the side of the bar is strongly influenced by the loading bar radius. Three bar radii are shown in Figure 2(b) $(r_b/R_s = 0.18,0.36,1.0)$. The peak value of τ is increased when the radius of the bar is decreased. In Figure 2(e) the distribution shear traction T_t along the *c*-*a* plane mid-way through the arterial section (r=t/2) is examined. Similar to the distribution of τ in the arterial material, T_t along a *c*-*a* plane is highest at the side of the loading bar ($S = \pi(r_b + d)/2$) and increases with decreasing value of r_b.

The effect of the radial coordinate of a *c*-*a* plane through the thickness was also examined, placing the plane a quarter-way through the thickness, such that the plane lies on S when $d = t/4$, results in a 7.3% decrease in T_t compared to $d = t/2$. However, placing the plane three quarters through the thickness, such that the plane lies on S when $d = 3t/4$, results in a 44% decrease in T_t. The plane lies on S when $d = t/2$ in Figure 2(d-f). Figure 2(f) shows the normal tractions (i.e. in the *r*-direction acting on a *c*-*a* plane) are negative (i.e. compressive) throughout the arch region and are negligible in the straight section of the specimen.

In terms of experimental design of a mode II fracture test, the analyses presented in Figure 2 provide the following insights:

- Maximum shear stress and shear traction on a *c*-*a* plane occur at the side of the loading bars ($S = \pi(r_b + d)/2$).
- A smaller loading bar generates highest magnitude of shear stress and shear traction on a *c*-*a* plane.
- Crack propagation along a *c*-*a* plane (as reported clinically) is expected to be pure mode II, based on computed compressive normal tractions throughout the arterial specimen.

We therefore select a small loading bar radius of 1.5 mm (corresponding to $r_b/R_s = 0.18$ for an aorta specimen radius of 8.33 mm).

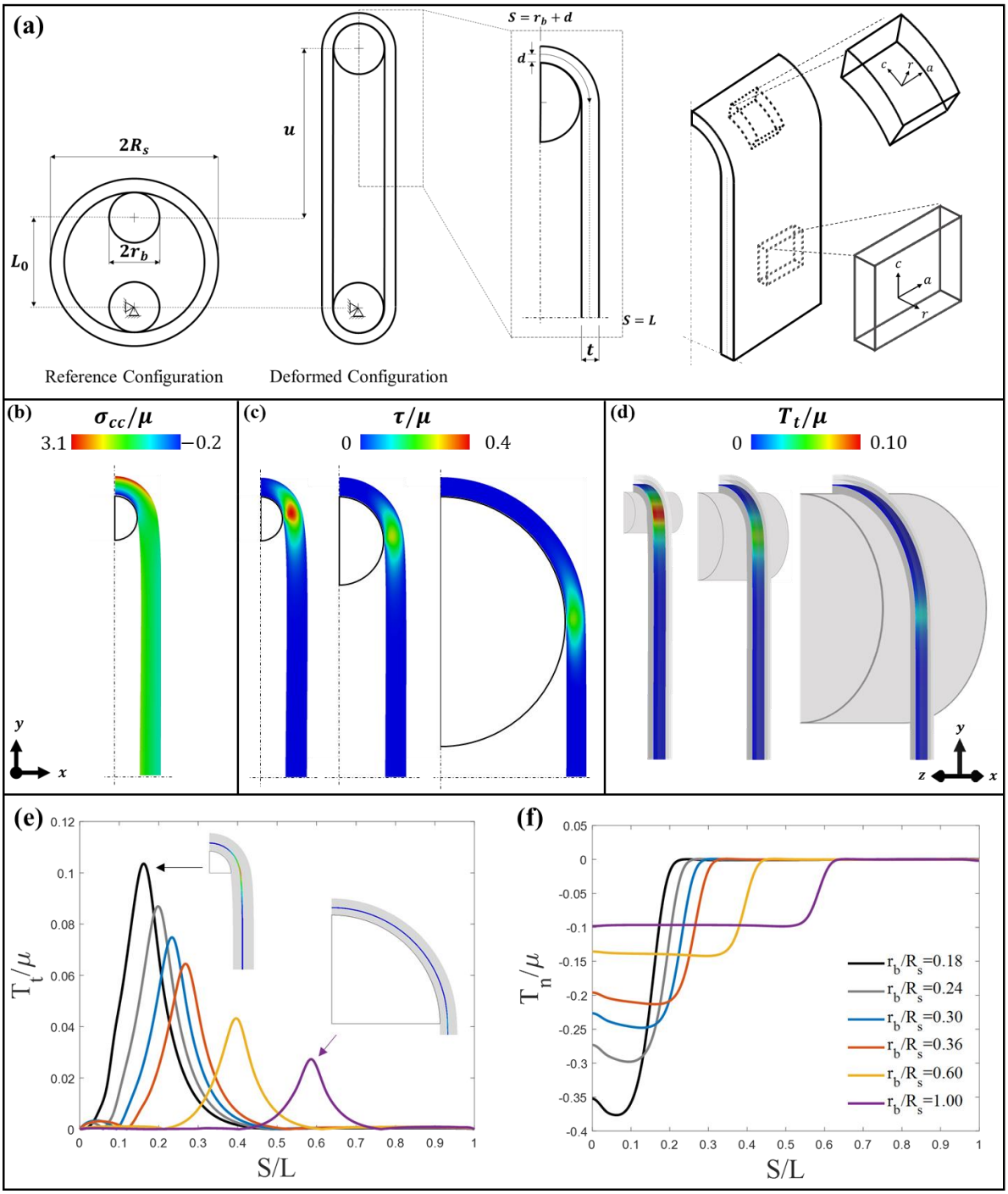

Figure 2. (a) Schematic of the *SFRT*. An excised aortic ring specimen is shown mounted on two bars in the reference configuration. R_s is the radius of the specimen and r_b is the radius of the bar. The bottom bar is fixed and u is the displacement of the top bar. S is the deformed interface coordinate which is a distance d offset from the bar. A schematic of the local material coordinate system is shown with local circumferential, axial, and radial directions (c-a-r); (b) Local circumferential stress is presented for a $r_b/R_s = 0.18$ configuration; (c) Maximum local shear stress (τ/μ) contour is plot for three bar radiuses ($r_b/R_s = 0.18, 0.36, 1.0$); (d) Normalised interface shear traction (T_t/μ) contour for the same radiuses as shown in (c); Tangential traction (e) and normal traction (f) as a function function of the normalised interface coordinate (S/L) for each of the bar radiuses analysed. Full details of the artery anisotropic hyperelastic material law used are presented in Appendix A.

We next hypothesise that the insertion of a notch in the radial direction at the location of maximum shear stress ($S = \pi(r_b + d)/2$), as illustrated in the schematic in Figure 3(a), will result in a kinking of the notch such that mode II initiation and propagation will occur along the c-a plane through the notch-tip, as shown in the illustrations of Figure 3(b) and Figure 3(c). Of course it is tempting to suggest that the notch should simply propagate in the radial direction through the sample without kinking, particularly given that the circumferential stress σ_{cc} (Figure 2(b)) is approximately five times higher than the

maximum shear stress (Figure 2 (c)). We explore these two competing hypotheses by simulating the deformation of the notched specimen while calculating the J-integral at the crack-tip for a radial crack path and for a circumferential crack path, as shown in Figure 3(b). The computed J-integral is significantly higher for a radial crack path than for a circumferential crack path; at an applied nominal circumferential strain of 0.9 it is 16 times higher. The underlying reason for this dramatic anisotropy in effective fracture toughness lies in the significant reorientation of collagen fibres behind the crack-tip (also shown in Figure 3(b)). In arterial tissue, collagen fibres lie along *c*-*a* planes. Therefore, collagen alignment due to increased circumferential strain acts as a toughening mechanism only for fracture in the radial direction (through the aligned fibres). Crack propagation in the circumferential direction does not benefit from the toughening mechanism of fibre alignment (essentially cracks propagate between the collagen). The results of Figure 3 support our hypothesis that our novel SFRT will result in kinking of the crack at the notch-tip, leading to mode II propagation in the circumferential direction through the *c*-*a* plane.

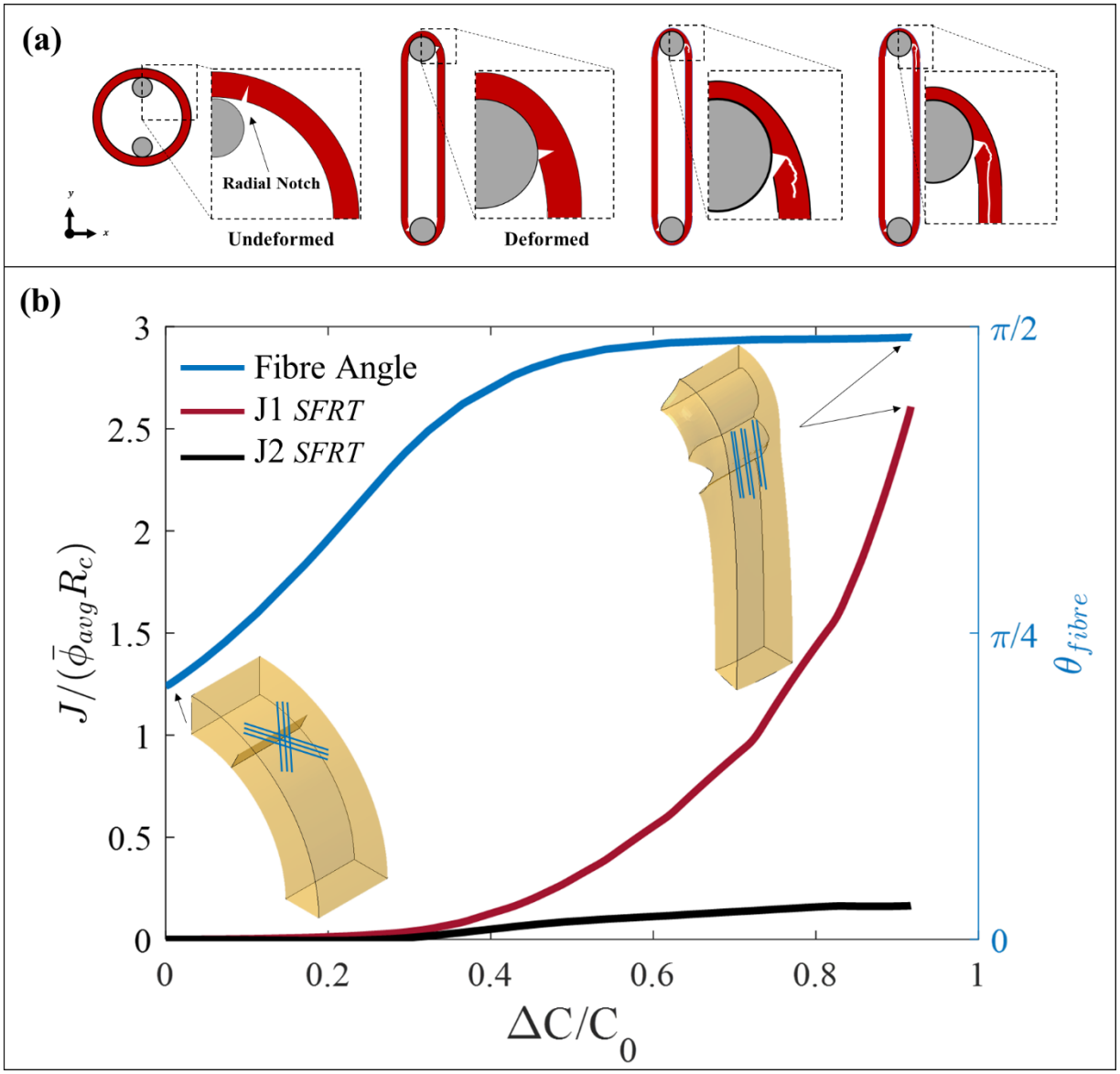

Figure 3. (a) Schematic of the proposed radial notch and the evolution throughout testing; (b) (left y-axis): J-Integral calculations for fracture paths in the radial and circumferential directions as a function of circumferential strain in a SFRT. Corresponding evolution of fibre alignment behind the crack-tip is also shown (right y-axis, blue curve) as a function of circumferential strain for the SFRT. (right y-axis): Fibre angle as a function of circumferential strain. Fibres are almost fully aligned in the *c*-direction at a circumferential strain of 0.6. A non-dimensional fracture resistance is presented as $J/(\bar{\phi}_{avg}R_c)$ where $\bar{\phi}_{avg}$ is the volume averaged strain energy density in the arterial tissue withing a radius R_c from the notch-tip. Note that $\bar{\phi}_{avg}R_c$ is identical for both crack paths so the figure presents a direct comparison of the J-integrals. Full details of the artery anisotropic hyperelastic material law used are presented in Appendix A.

Finally, in Figure 4, using a choesive zone formulation (described in Appendix A), we examine the mode mixity during crack initiation and propagationin our *SFRT* test. Motivated by the results of the analysis presented in Figure 3, we again consider a radial notch positioned at the point of maximum shear and we place a cohesive surface along the *c*-*a* plane through the notch-tip. Simulated crack initiation and propagation is presented in Figure 4. The evolution of T_t along the *c*-*a* plane through the notch tip (r=t/2) is shown in Figure 4(a), in addition to the computed specimen deformation. Following initiation at the side of the loading bar ($S = \pi(r_b + d)/2$), at an applied circumferential strain of $\Delta C/C_0 = 0.64$, the crack front propagates a long distance along the *c*-*a* plane. The delaminated portion of artery (i.e. the evolving crack flank) remains flat on the *c*-*a* plane, suggesting that the crack growth is pure mode II throughout. This is confirmed by plotting the mode mixity φ_{MM} at the crack-tip as a function of crack-tip position during propagation, as shown in Figure 4(b). Corresponding plots for lap-shear test simulations are shown once-again for comparison, highlighting the significant improvement of the SFRT in generating mode II initiation and propagation in arterial tissue. The normal interface calibrated from standard peel tests (see supplementary material I) is $\sigma_{max} = 202\ kPa$.

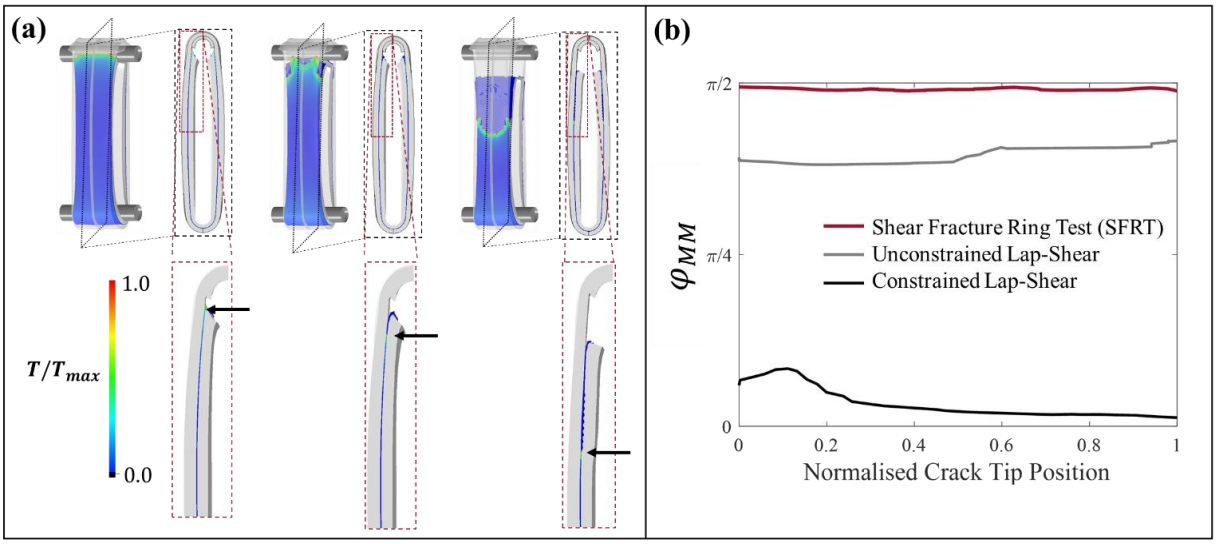

Figure 4. (a) Section views of the finite element simulation of the *SFRT* carried out in the present study. Sections are taken in the middle of the aortic ring as the crack propagates. Crack tip is shown by the black arrow; (b) Mode mixity (ϕ_{MM}) as a function of normalised crack tip position for each of the shear experiments analysed in this study. Cohesive zone parameters are as follows: the normal interface strength is calibrated from peel tests, $\sigma_{max} = 202\ kPa$ (see supplementary material I); the shear interface strength is assumed to be approximately twice the normal interface strength, $\tau_{max} = 400$ kPa; the mode I and mode II fracture energies are assumed to be $G_n^0 = 0.003\ N/mm$ and $G_t^0 = 0.003\ N/mm$. Full details of the cohesive zone model are presented in Appendix B.

Following from the key computational design and analysis presented in Figures 2-4, a proposed experimental test rig is shown in Figure 5(a). Cantilevered stainless steel loading bars are attached to the base-plate and the cross-head fixture of a mechanical test machine. Selection of loading bar radius is a key design consideration. While, as shown above, a smaller radius enhances the level of shear stress, bars must be large enough to support the forces imposed by the deforming arterial specimen without exceeding the elastic limit of stainless steel. The force imposed by the deforming specimen is, of course, dependent on the chosen specimen width, w. Specimens are prepared such that $w/t \approx 4.14$, so that specimens are sufficiently wide to approximate generalised plane strain conditions, but not so wide that significant anatomical variations are introduced in the a-direction (i.e. specimens are approximately cylindircal). For a typical specimen thickness of t=2.35 mm, a width w=9.73 mm is chosen. Specimens are placed as close as possible to the cantilevered ends of the loading bars (while contacting only the loading bars). Preliminary testing suggests that a specimen exerts a uniformly distributed load of ~0.97 N/mm on the loading bars at ~$\Delta C/C_0 \approx 0.6$ prior to rupture. Figure 5(a) shows the stress in stainless steel loading bars, normalised by the yield stress of stainless steel (200 MPa). Clearly, a bar radius in the range $r_b/R_s \leq 0.135$ (corresponding to $r_b \leq 1.125\ mm$ based on a mean artery radius of 8.33 mm) does not provide an adequate factor of safety for the structural integrity of the loading bar. On the otherhand, large bar radii $r_b/R_s \geq 0.25$ result in lower magnitudes of shear stress and, consequently, a reduced probability of mode II fracture. Therefore a bar of radius $r_b/R_s = 0.18$ (i.e. $r_b = 1.5\ mm$) is chosen to provide a high level of shear stress while ensuring that the yield stress of the loading bar is not exceeded. This bar size also facilitates straight-forward positioning of the radial notch at the position of maximum shear to the side of the bar ($S = \pi(r_b + d)/2$). A high-resolution camera (60 fps, 1080p) and digital microscope (10 fps, 1080p) are positioned in front of the sample to record specimen deformation and crack propagation throughout each test. A photograph of the final test set-up is shown in Figure 5(c).

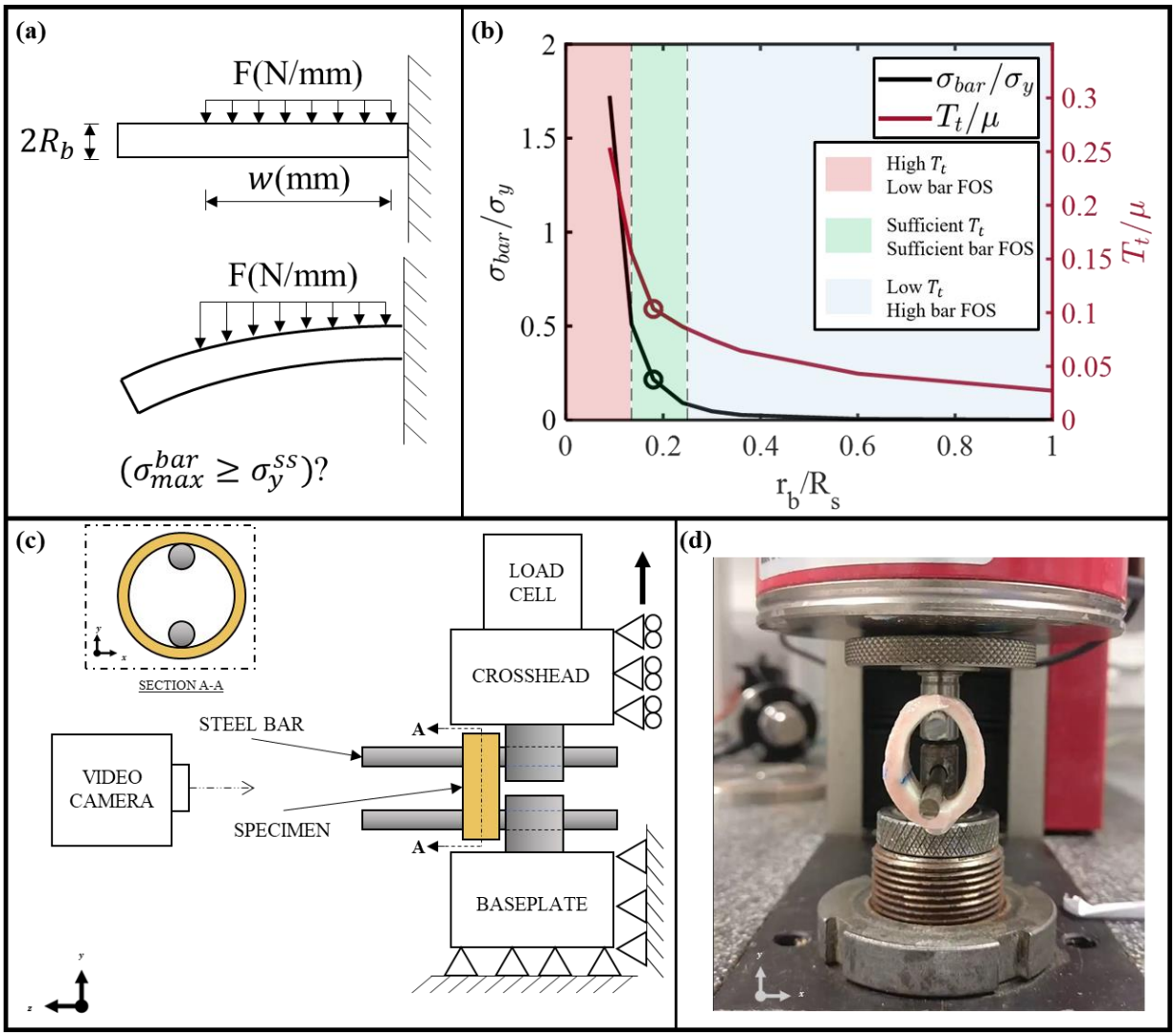

Figure 5. (a) Schematic of structural bending of loading bar during stretching of artery SFRT specimen; (b) Identification of optimal experimental design based on required loading bar flexural strength and generation of high shear stress in arterial tissue. The blue shaded region indicates a high loading-bar factor of safety (FOS) and low shear traction. The red region indicates a low loading-bar FOS and a high shear traction. The green region indicates the optimal experimental design whereby high shear tractions are generated in the artery while a sufficiently high loading-bar FOS is achieved; (c) Schematic of the computationally designed experimental test rig. The section view (Section A-A) shows the front view of the specimen; (d) Finalised test-rig design with mounted arterial SFRT specimen.

2.1 Sample Preparation

The ascending aorta and aortic arch were excised from 6 sheep sourced from a local abattoir (Brady's Athenry, Galway, Ireland). Excess connective tissue was carefully removed from the external (adventitial) surface of the vessel. Notched and un-notched specimens were prepared through cutting cylindrical sections out of the aorta to form circumferentially intact rings. Sample dimensions were taken using a digital Vernier callipers and a digital thickness gauge. Tissue samples were stored at 0-4℃ in phosphate buffer solution prior to testing to ensure adequate tissue hydration and preservation. Unnotched intact ring extension tests (n=6) and notched ring extension tests (n=11) were carried out. Samples were mounted on a rigid bar to allow for constrained, precise notching. Two notches were introduced using a No. 10 scalpel blade at opposite ends of the sample. Notches were approximately a half of the tissue thickness in depth ($r_{ct} \approx t/2$). The boundary of the notch was marked with blue waterproof all-surface ink. Samples were mounted on the extension bars and tested to failure at a strain rate of 10 mm/minute. The samples were rotated such that the notches were aligned with $S = \pi(r_b + d)/2$.

To determine the anisotropic hyperelastic properties and anisotropy of the material, three experiments were carried out: axial extension, circumferential extension, and unnotched intact ring extension. Uniaxial testing in two directions was carried out rather than biaxial testing due to the non-uniform strain states in biaxial samples [22]. Strips were excised from the

ascending aorta and cut to uniform rectangular shapes in the axial and circumferential directions maintaining a mean aspect ratio of $L{:}\,w = 3.8{:}\,1$ (all mean specimen dimensions are presented in Table 1). The samples were gripped using Zwick pneumatic specimen jaws. Axial (n=10) and circumferential (n=6) extension tests were carried out individually with a crosshead speed of 10 mm/min. Each of the samples were tested to failure.

Table 1. Mean specimen dimensions ± SD for each of the experiments. Reported values for SFRT length and unnotched intact ring extension length refer to the diameter of the specimen pre-test. Circumferential extension length is the initial grip to grip separation. *Peel test experiment is presented in supplementary material I.

Experiment	Length or Radius (mm)	Width (mm)	Thickness (mm)
Peel Tests* (n=7)	37.96 ± 6.59	12.77 ± 1.07	1.95 ± 0.5
Circumferential Extension (n=6)	19.06 ± 2.28	4.60 ± 1.17	1.39 ± 0.16
Axial Extension (n=10)	27.68 ± 4.35	7.89 ± 0.92	2.06 ± 0.33
Unnotched Intact Ring Extension (n=7)	8.85 ± 0.23 (R_s)	5.15 ± 0.49	2.05 ± 0.14
SFRT (n=11)	9.09 ± 0.60 (R_s)	9.73 ± 2.32	2.35 ± 0.16

3 Results

3.1 Determination of Hyperelastic Properties

Prior to simulation of fracture experiments, the anisotropic hyperelastic behaviour of the arterial tissue must first be calibrated using uniaxial tension testing of the tissue in the circumferential and axial directions, as described in Section 2.1. Additional validation of the calibrated material model is performed by experimental and computational analysis of the response of unnotched artery sections to our *SFRT*. Experimental tensile testing reveals significant anisotropy and material non-linearity, as shown in Figure 6*a*. The material exhibits a higher initial stiffness in the circumferential direction. Furthermore, in the circumferential direction the material transitions to a high stiffness regime at a strain of ~0.4. Strain stiffening is less pronounced in the axial direction. The model provides an accurate representation of the material anisotropy and strain stiffening both in the circumferential direction ($RMSE_{circ} = 0.0059$) and in the axial direction ($RMSE_{axial} = 0.0144$) for the unique material parameter set presented in Table 2. Simulation of the stretching of an unnotched intact ring using the calibrated material model parameters, is shown in Figure 6(b). Results are in strong agreement with corresponding experimental measurements for the entire range of applied deformation ($RMSE_{ring} = 0.0081$).

Table 2. Table of best fit material parameters for the arterial material model.

D_1^m	D_2^m	E_1^m (MPa)	E_2^m (MPa)	**K** (MPa)	D_1^f	D_2^f	E_1^f (MPa)	E_2^f (MPa)	$\alpha(^\circ)$	β
0.15	0.9	0.075	0.5	1.52	0.4	0.5	0.16	4.5	28.5	15.0

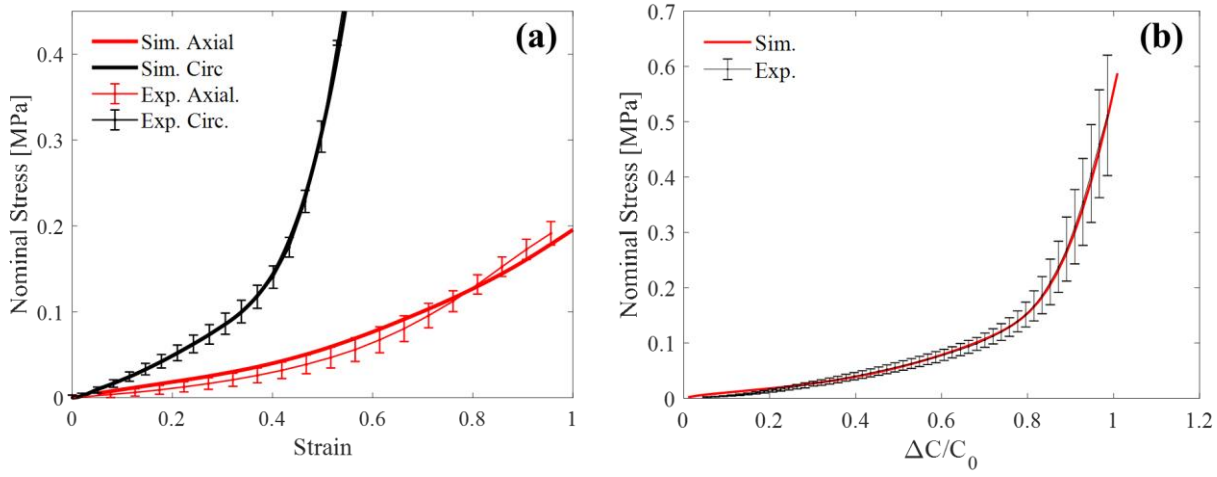

Figure 6. (a) Nominal stress (MPa) as a function of nominal strain for the uniaxial extension of the axial and circumferential datasets. Experimental data and numerical data are shown. The root mean squared error (RMSE) of the axial and circumferential data sets are 0.0144 and 0.0059 respectively; (b) Nominal stress (MPa) as a function of the circumferential strain for the unnotched intact ring extension tests. RMSE for the unnotched intact ring extension test is 0.0081. Final material parameters are presented in Table 2. Full details of the artery anisotropic hyperelastic material law are presented in Appendix A.

3.2 Fracture Mechanics results

Firstly, we introduce the results of our SFRT fracture mechanics investigation by presenting the details of a representative aorta test sample, Figure 7 shows the measured force (F/wt) versus applied nominal circumferential strain ($\Delta C/C_0$). The measured force continues to increase beyond the point of crack initiation at $\Delta C/C_0 = 0.72$. This is due to the continued load bearing capacity of the outer section of the ring ($r > r_{ct}$) up to the point of ultimate rupture.

Fracture initiation (shown in Figure 7(a)) appears to be a pure mode II initiation with no evidence of normal separation of the fracture surfaces at the crack-tip; i.e. fracture initiation entails an immediate kinking of the radial notch so that a mode II initiation along the *c*-*a* plane occurs. This experimental results confirms the key insight provided by the J-integral calculations presented in Figure 3, and demonstrates that toughening mechanisms due to fibre alignment behind the crack-tip will result in crack kinking and mode II fracture along the *c*-*a* plane, rather than mode I fracture along the *r*-*a* plane. Following initiation, significant crack propagation is observed in the *c*-direction through the *c*-*a* plane over a long distance (Figure 7(a-d)). This crack propagation appears to be close to pure mode II with no visible normal separation at the crack-tip. A relatively smooth fracture surface is observed along the *c*-*a* plane and the crack flank (delaminated material) is observed to remain flat to the *c*-*a* plane throughout the test. As shown in Figure 7(b), at $\Delta C/C_0 = 0.86$, propagation appears to be a pure mode II in nature. This pattern of mode II propagation continues through $\Delta C/C_0 = 0.93$ (Figure 7(c)) up to, and including, the point of ultimate rupture ($\Delta C/C_0 = 0.97$; Figure 7(d)). This observed pattern of mode II initiation and propagation in the *c*-direction along the *c*-*a* plane is remarkably similar to that predicted by experimental design calculations (Figure 2 and Figure 3). This exact pattern of mode II initiation and propagation was observed in all samples (n=11) subjected to our novel SFRT test. In no case was mode II cracking in the *r*-direction observed, despite the high levels of circumferential nominal strain applied to the specimen during our SFRT tests. This highlights the benefit of detailed computational analysis to uncover competing mechanism of material damage when designing biomechanical tests for biological materials.

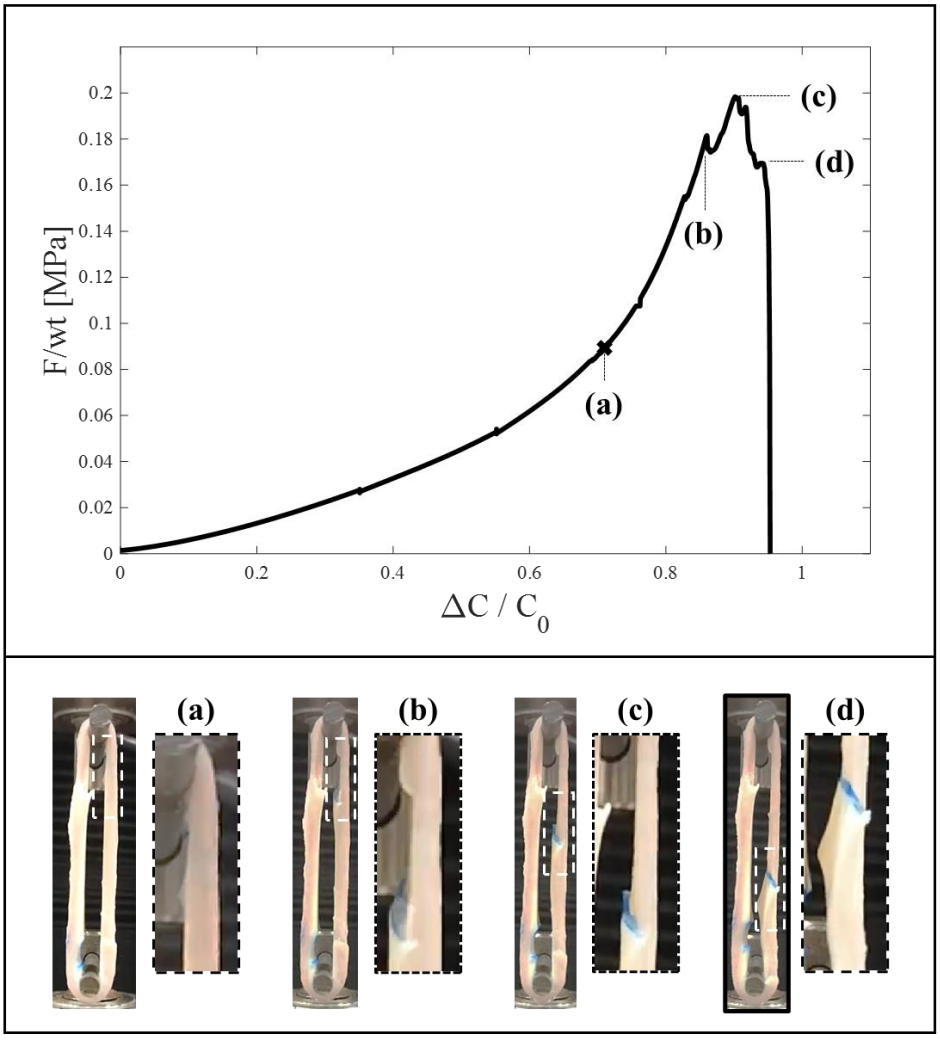

Figure 7. The graph shows force normalised by the cross-sectional area, F/wt (MPa) as a function of the circumferential strain

($\Delta C/C_0$). The point of crack initiation is marked with an X. Experimental results of the *SFRT* for a representative sample. (a-d) Progression of the crack tip from the point of initiation to ultimate rupture of specimen (S3). The original notch is seen in blue.

Figure 8 shows the measured force (F/wt) versus applied nominal circumferential strain ($\Delta C/C_0$) for all SFRT samples (n=11). Points of crack initiation are indicated for all cases. As stated above, mode II crack propagation in the c direction through the c-a plane is observed in all cases. Generally, fracture initiation is observed to occur in the transition between the initial low stiffness regime and the high stiffness regime. The range of nominal strain at initiation is observed as $0.53 \leq \Delta C_i/C_0 \leq 0.82$; mean$\pm$SD=0.64$\pm$0.23. This illustrates the quantitative repeatability of the SFRT methodology, despite high levels of inter-sample variability typically reported for mechanical behaviour of aortic tissue. Finally, in all samples (n=11), crack initiation does not eliminate the load bearing capacity of the specimen due to the intact outer layer of each specimen ($r > r_{ct}$). However, superposition of the corresponding mean curve for an intact unnotched specimen subjected to the same loading regime (Figure 8) confirms that the presence of the notch, and consequent mode II crack propagation, leads to a reduction in measured force throughout each test.

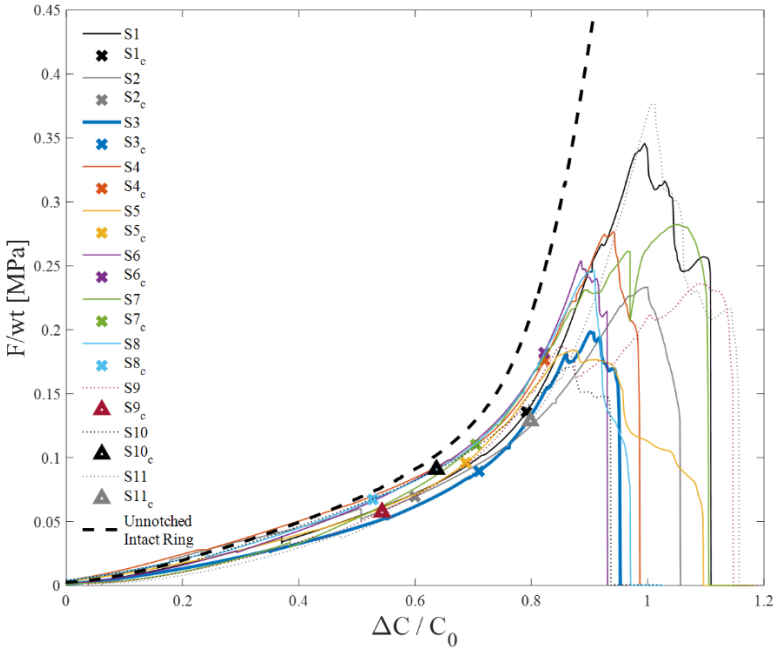

Figure 8. Force normalised by the cross-sectional area, F/wt (MPa) as a function of the circumferential strain ($\Delta C/C_0$) for each of the radial notch test specimens. The points of crack initiation are marked with the symbol shown in the legend and are denoted by Sn_c where n is the specimen number. The mean stress strain data for the unnotched intact ring extension test is shown as the thick dotted black line. The notched samples exhibit a lower stiffness in the high strain regime compared to the unnotched intact ring.

Figure 9 shows the deformed crack length as a function of applied deformation beyond the point of initiation ($(\Delta C - C_i)/C_i$). The mean final deformed crack length was 22.65$\pm$9.68 mm. The typical fracture pattern is characterised by a regime of slow crack growth post-initiation followed by a regime of rapid growth. One likely cause for the initial slow growth followed by the rapid growth is the experimentally observed fibrillation during early stages of crack growth. Extension and pull-out of fibres between fracture surfaces will provide partial resistance to crack propagation. In 4 samples, a third regime of further slow crack growth subsequent to the fast growth regime is observed.

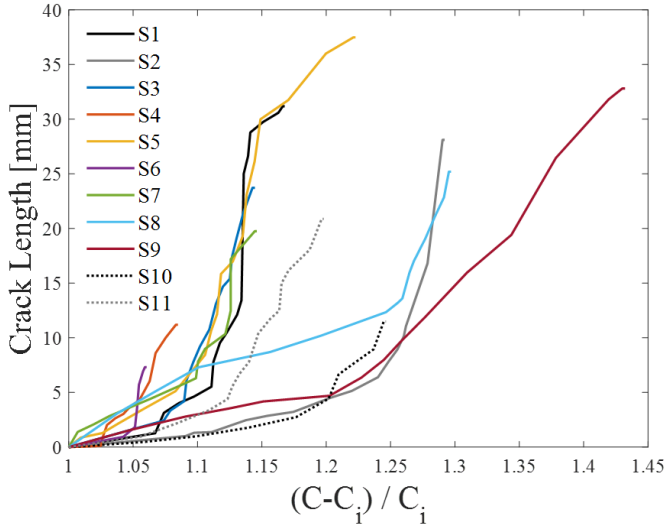

Figure 9. Crack length as a function of circumferential stretch past initiation. $(C - C_i)/C_i = 1$ indicates the point of crack initiation and the final point on each curve is the point at which the specimen underwent final rupture.

Images of the fracture surfaces are shown for eight samples in Figure 10. The original notch is marked with blue ink in each of the images. Images confirm that crack propagation is restricted to the same *c*-*a* plane (through the original notch-tip) for the entirety of the test, up to the point of final rupture, again confirming the mechanism of mode II fracture predicted in our design of experiment calculations (Figure 2 and Figure 3). Fibrillation is observed at the crack-tip at the end of SFRTs, as shown Figure 10(h), in addition to the early stages of fracture propagation and initiation.

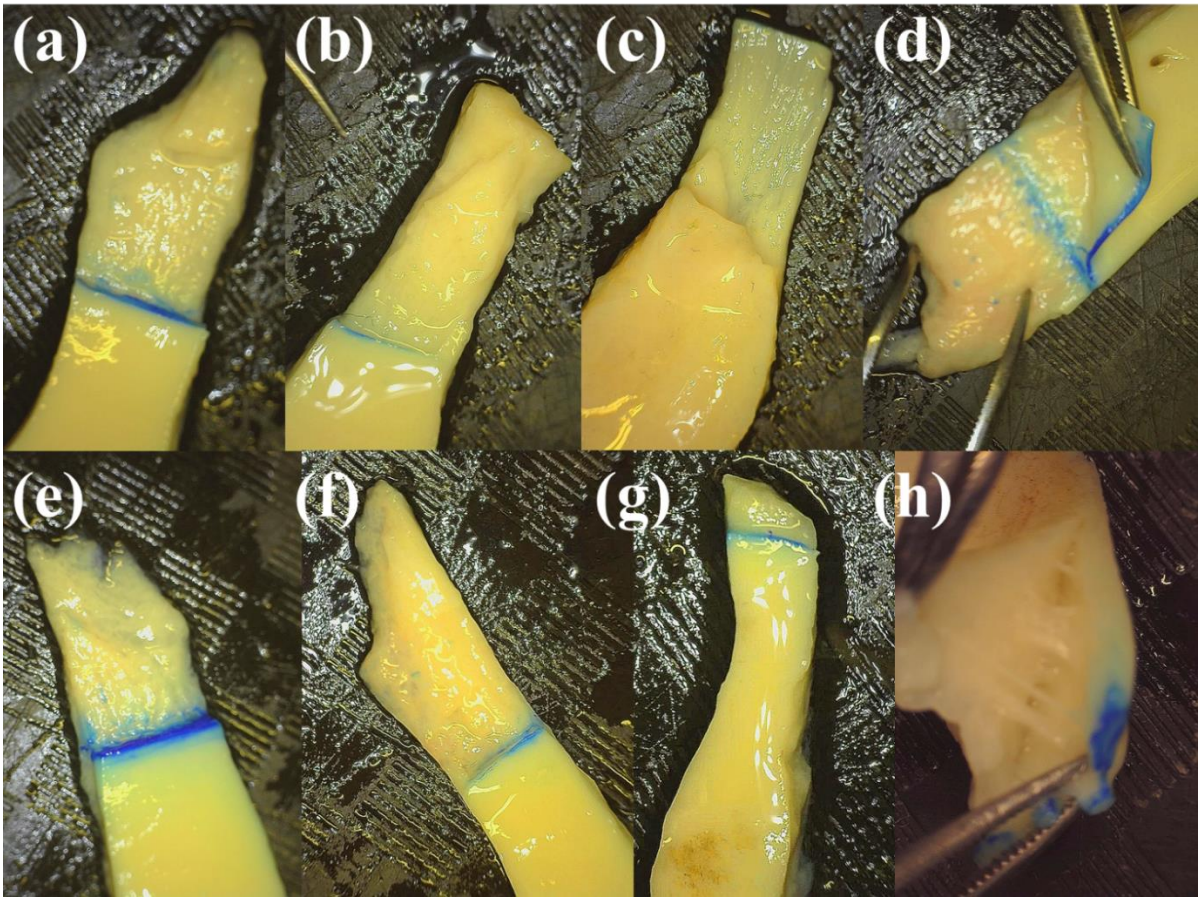

Figure 10. Fracture surfaces of the specimens. Original notches are shown with blue ink. Fibrils formed during fibrillation are shown in (h).

3.2.1 Computational analysis of SFRT experiments to determine mode II fracture properties

Deformed finite element meshes during crack initiation and propagation are shown in Figure 11(a). In all simulations the mixed-mode CZM described in Appendix A is implemented. The value of the parameter σ_{max} of $202\ kPa$ (the mode I fracture strength along the *c-a* plane) is determined from the implementation of standard peel test experiments, described in Appendix B. The sensitivity of SFRT crack initiation to the mode II fracture strength, τ_{max}, is presented in Figure 12(b). τ_{max} values of 1.4 MPa and 1.8 MPa predict fracture initiation within the experimentally observed standard deviations (in terms of circumferential strain and measured force), and a value of $\tau_{max} = 1.6$ MPa leads to the prediction at $\Delta C/C_0 = 0.63$ and $F/wt = 0.84\ MPa$, which is within 0.86% of the experimentally measured mean values of $\Delta C/C_0 = 0.63$ and $F/wt = 0.84\ MPa$, respectively. This suggests that the mode II fracture strength for initiation along the *c-a* plane is eight times higher than the corresponding mode I strength along the *c-a* plane. It should be emphasised that this is not reflective of the mode I strength for fracture along the *r-a* plane, as demonstrated by the J-integral analysis presented in Figure 3, which we expect to be considerably higher than τ_{max} or σ_{max} along the *c-a* plane. Similar to experimental measurements, the computed force (F/wt) increases following fracture initiation. Additionally, similar to experiments, computed forces for notched SFRTs are lower than corresponding curves without the presence of a notch/crack propagation.

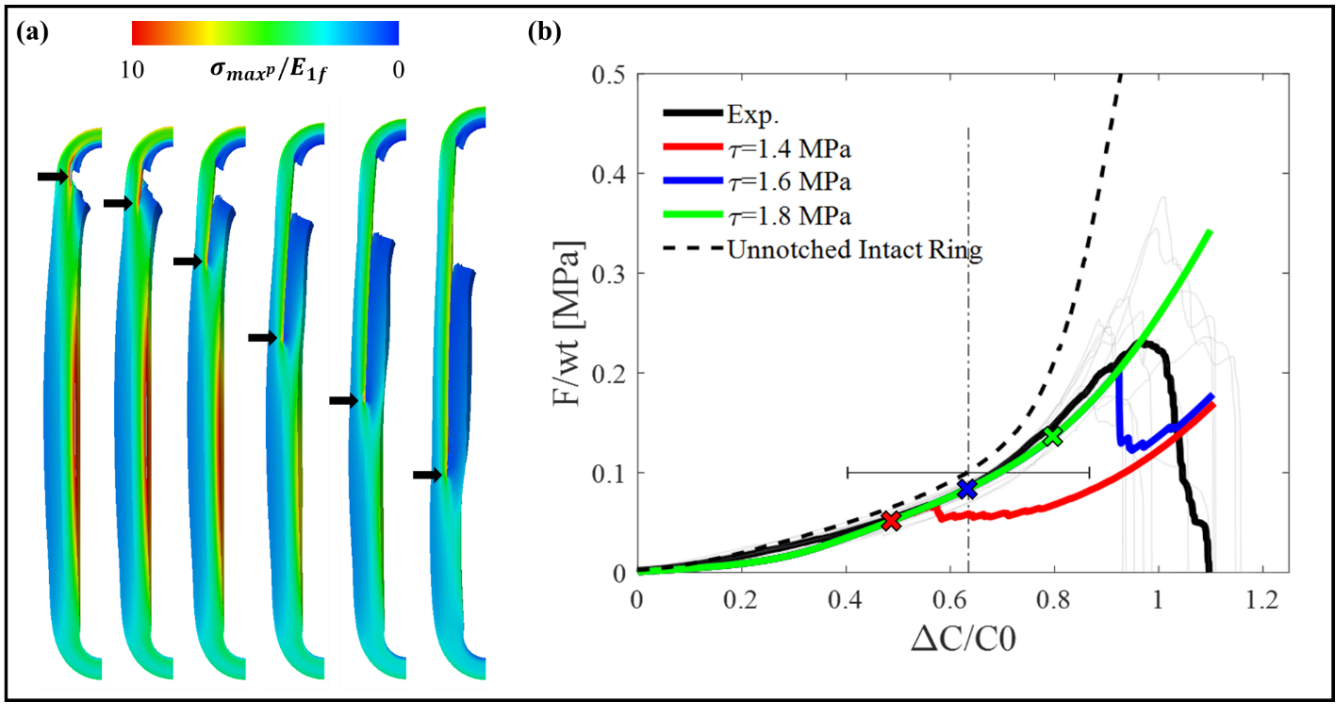

Figure 11. (a) Contour plot of max principal stress showing the progression of a mode II crack propagation, black arrows indicate the area of the crack tip; (b) Sensitivity of the crack initiation to the mode II interface strength. Mean force normalised by the cross-sectional area as a function of circumferential strain ($\Delta C/C_0$) for the SFRT. Points of crack initiation are shown with an 'X'. In each simulation the mode I interface strength was $\sigma = 202\ kPa$, the mode II fracture energy was $G_t^0 = 0.001\ N/mm$, and the mode I fracture energy was $G_n^0 = 0.001\ N/mm$. The mean circumferential strain ($\Delta C/C_0$) at initiation is shown by the vertical dotted black line and the standard error is the shown by the horizontal error bar. Full details of the artery anisotropic hyperelastic material law and cohesive zone model are presented in Appendix A and Appendix B, respectively.

While the point of fracture initiation is highly sensitive to the parameter τ_{max}, it is not found to be sensitive to the mode II fracture energy (G_t^0). However, as shown in Figure 12, simulations reveal that the rate of crack propagation exhibits sensitivity to G_t^0. Simulations reveal that a value of $G_t^0 = 0.25$ N/mm results in a rate of crack propagation that is slower than that observed experimentally. On the other end of the spectrum, values of $G_t^0 \geq 0.0005$ N/mm result in excessively high rates of propagation compared to experimental measurements. A value of $G_t^0 = 0.005$ N/mm is predicted to provide a reasonable approximation of experimental measurement, both during early and later stages of crack initiation.

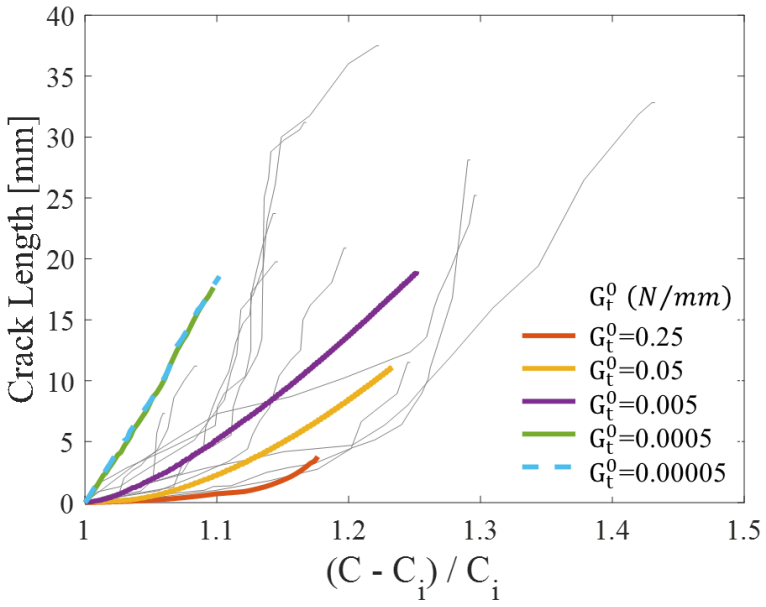

Figure 12. Simulated crack length as a function of circumferential stretch past initiation presented alongside the experimental data (shown in light grey). The crack length and velocity are shown to depend on the mode II fracture energy. Cohesive zone parameters are $\sigma_{max} = 202\ kPa, \tau_{max} = 1.6\ MPa$, the mode I fracture energy is scaled with the mode II fracture energy according to $G_n^0 = (\sigma_{max}/\tau_{max})G_t^0$. Full details of the artery anisotropic hyperelastic material law and cohesive zone model are presented in Appendix A and Appendix B, respectively.

4 Discussion

The current study presents the development and implementation of a novel experimental technique (SFRT) to generate and characterise mode II crack initiation and propagation in arterial tissue. A mechanistic consideration of a large body of clinical studies suggest that artery dissection results from mode II initiation and crack propagation along a *c*-*a* plane in the artery wall, rather than mode I propagation. However, the majority of artery fracture experiments rely on mode I peel test. Recently the studies of Sommer et al. [17] and Witzenburg et al. [16] adopt standard lap-shear test techniques to measure mode II fracture properties. The current study begins with a demonstration that lap-shear testing of arterial tissue results in mixed mode fracture, rather than mode II due to the high levels of tissue deformation at the crack-tip at the point of initiation. The combination of high toughness and high deformability of arterial tissue presents a considerable challenge in generating mode II fracture. A further challenge, albeit an obvious one, is that fracture testing of naturally occurring biological materials such as arteries does not facilitate the engineering of standardised fracture specimen geometries. Therefore, implementation and interpretation of fracture testing subject to the limitation of non-standard geometries such as arteries requires in-depth mechanistic analysis. In the current study we perform a detailed computational design of a novel experimental method (which we refer to as a shear fracture ring test (SFRT)) to robustly and repeatably generate mode II crack initiation and propagation in the *c*-*a* plane of arteries. This method is based on generating a localised region of high shear adjacent to a cylindrical loading bar. Placement of a radial notch in this region of high shear stress is predicted to result in a kinking of the crack during a mode II initiation and propagation of the crack over a long distance in the *c*-direction along the *c*-*a* plane. A J-integral analysis suggests radial mode I crack propagation will not occur due to significant fracture toughening as a result of collagen alignment in the *c*-direction behind the crack-tip. Fabrication and experimental implementation of the SFRT on excised ovine aorta specimens confirms that the novel test method results in pure mode II initiation and propagation, as predicted by our computational design of experiment. Using a cohesive zone formulation, we simulate our mode II experimental tests and we demonstrate that the mode II fracture strength along the *c*-*a* plane is eight times higher than the corresponding mode I strength determined from a standard peel test. We also calibrate the mode II fracture energy based on our measurement of crack propagation rates. The mechanisms of fracture uncovered in the current study, along with our quantification of mode II fracture properties have significant implications current understanding of the biomechanical conditions underlying in vivo aortic dissection.

The present study provides an explanation why every dissection is associated with circumferential and axial crack propagation, but not always radial (i.e. the majority of aortic dissections do not rupture [11,13]). Aortic rupture requires radial crack propagation, and collagen fibre alignment provides high levels of toughening against radial fracture. The results of this study suggest radial crack propagation is only likely to occur between collagen fibres or in areas where there is less fibre toughening. The majority of aortic dissection-induced ruptures occur in the ascending aorta leading to cardiac tamponade and

death [11,23]. This may be due to the discontinuous and irregular collagen structure observed in the wall of ascending aortic dissections [24,25]. Such irregular and discontinuous structure reduces the radial toughening mechanism in the aortic wall. This is also a possible mechanistic explanation for the high incidence of aortic dissection amongst patients with connective tissue diseases such as Marfan syndrome and Ehler-Danlos syndrome [26–29]. Connective tissue disorders significantly alter the intramural and inter-lamellar aortic microstructure and strength through abnormal fibrillin (Marfan), and collagen deterioration (Ehler-Danlos). This puts patients with connective tissue disorders at higher risk of aortic dissection [30,31].

The propagation of a pure mode II crack following insertion of a notch is suggestive that the intimal tear or initiation tear acts in a similar fashion *in vivo* to the notch [2]. The notch acts as a concentrator of stress at the notch tip and causes shear stress localisations [32]. The notch also significantly reduces the strain in the inner layer of the artery relative to the outer layer which results in a shear concentration. The results of the present experiment serve as supporting evidence to the theory that aortic dissection is far more likely to occur in the presence of an intimal tear [33,34]. This is highlighted further by the additional testing carried out using circumferential notches (see appendix B). Only 3 of the 8 samples tested with circumferential notches resulted in mode II crack propagation, indicating crack growth in the aorta is much more likely to occur in the presence of a radial tear or notch.

The cohesive zone model used in the present study allows for the accurate calibration of a mode II interface strength and mode II fracture energy. However, it is not capable of capturing the complex rate-dependant plastic nature of the fracture, this is reflected in the predicted crack lengths which are linear and do not sufficiently capture the two crack growth regimes (fibrillation and rapid crack growth). Future work should focus on the development of a rate-dependant cohesive zone model capable of capturing the complex nature of viscoplastic fibrillation in soft tissues. The cohesive zone parameters calculated in the present study should be applied to patient-specific geometries to assess the risk of dissection. They should also be used to examine a range of biomechanical factors which may influence arterial dissection. A companion study to the present study is currently underway examining the application of these CZM parameters to an MRI derived subject-specific aortic geometry to analyse the risk of aortic dissection.

The test methodology (*SFRT*) developed in the present study could readily be applied to large veins such as the pulmonary veins or other large arteries (left subclavian artery, left common carotid artery, brachiocephalic artery, iliac arteries, renal arteries). The apparatus could be scaled to work on coronary arteries, femoral arteries, carotid arteries, and other arteries of a similar size). Furthermore, it could potentially be used with any other tubular soft tissue of interest such as the urethra, bronchial tubes, trachea, and skin to name but a few.

Appendix A: Artery Material Model

In order to simulate the anisotropic non-linear hyperelastic behaviour of arterial tissue we use a recently proposed formulation by Fereidoonnezhad and McGarry. Full details are presented in Fereidoonnezhad et al. (under review, *Journal of Biomechanics*), including extensive demonstration that this new formulation robustly avoids the computation of non-physiological auxetic behaviour during large deformation of anisotropic soft tissue, in contrast to established formulations. Here we briefly present the key features of the model and we demonstrate that it accurately captures the mechanical behaviour of the ovine arterial specimens used in this study. The anisotropic strain energy density function for the i^{th} fibre-family is given as:

$$\Psi_{fi} = \begin{cases} E_{1f}\left(\frac{2}{3}\lambda_{fi}^3 - \lambda_{fi}^2 + \frac{1}{3}\right), & \lambda_{fi} - 1 \le D_{1f} \\ \frac{2}{3}\lambda_{fi}^3(q-2p) + \frac{p}{2}\lambda_{fi}^4 + \lambda_{fi}^2(p-q+r) + \psi_{01}, & D_{1f} < \lambda_{fi} - 1 < D_{2f} \\ \frac{2E_{2f}}{3}\lambda_{fi}^3 + \lambda_{fi}^2\left(pD_{2f}^2 + qD_{2f} + r - E_{2f} - E_{2f}D_{2f}\right) + \psi_{02}, & \lambda_{fi} - 1 \ge D_{2f} \end{cases} \quad \textbf{(A1)}$$

This component consists of three regimes: a low stiffness regime where fibres are coiled/wavy at low strain; a transition regime to describe the strain stiffening of fibres as they become less wavy during extension; a high stiffness regime in which straightened fibres exhibit a high elastic stiffness. λ_{fi} is the fibre stretch of the i^{th} fibre-family, E_{1f} and E_{2f} are fibre stiffness values in the low and high stiffness regimes, respectively. D_{1f} and D_{2f} specify the stretch at the beginning and end of the transition regime. The remaining non-independent model coefficients are required to ensure C^0 and C^1 continuity of fibre stress and energy.

A similar tri-regime formulation is specified for the isotropic matrix component of the model: And the strain energy density function of the isotropic matrix contribution is given as:

$$\Psi_{iso}(\bar{\lambda}_i) = \frac{E_{2m} - E_{1m}}{f(D_{2m}) - f(D_{1m})} h(\bar{\lambda}_i) + \left(E_{1m} - \frac{E_{2m} - E_{1m}}{f(D_{2m}) - f(D_{1m})} f(D_{1m}) \right) (\bar{\lambda}_i - ln\, \bar{\lambda}_i)$$

$$f(\bar{\lambda}_i) = \text{erf}\left(\frac{2\bar{\lambda}_i - 2 - D_{1m} - D_{2m}}{2\sqrt{2}\beta} \right) \quad \textbf{(A2)}$$

in which the function $h(\bar{\lambda}_i)$ is derived by the double integration of $f(\bar{\lambda}_i)$, $\bar{\lambda}_i, i = 1,2,3$ are the eigenvalues of the isochoric deformation gradient (modified principal stretches), and D_1 and D_2 are the stretches at the beginning and the end of the transition regime. E_1 and E_2 are the matrix stiffness values in the low and high stiffness regimes, respectively. The slight material compressibility is based off of the experiments of Nolan and McGarry [35]. For further information regarding the material model the reader is directed to Fereidoonnezhad et al. (under review, *Journal of Biomechanics*). A *user defined material subroutine* (UMAT) has been developed for this formulation so that it can be implemented in the Abaqus finite element solver.

Appendix B: Cohesive Zone Fracture Model Description

To model the delamination at the interface we implement a fully coupled mixed-mode cohesive zone model. For a given interface displacement vector (with normal and tangential (shear) components Δ_n and Δ_t, respectively) the magnitude of the interface traction is given as:

$$T_m(\Delta_n, \Delta_t) = \begin{cases} K_m \Delta_m \,, \Delta_m < \delta_m^{el} \\ K_m \delta_m^{el} (1 - D) \,, \Delta_m \geq \delta_m^{el} \end{cases} \quad \textbf{(B1)}$$

where K_m is the interface stiffness, Δ_m is the magnitude of the interface displacement vector, and δ_m^{el} is the maximum separation prior to the initiation of damage. Interface damage, D, increases monotonically from 0, at the onset of damage, to 1, at the point of ultimate failure, such that:

$$1 - D = \exp\left(-\frac{\Delta_m^{max} - \delta_m^{el}}{\delta_m^*} \right) \frac{\Delta_m}{\Delta_m^{max}} \quad \textbf{(B2)}$$

Δ_m^{max} is the displacement magnitude at ultimate failure; δ_m^* governs the rate at which damage increases with increasing interface displacement. The maximum separation prior to the initiation of damage is defined as a function of the mode angle ($\varphi_{MA} = \tan^{-1}(\Delta_t / \Delta_n)$) as follows:

$$\delta_m^{el}(\varphi_{MA}) = \frac{\tau_{max}}{K_m} - \kappa_1 \left(1 - \exp\left(-\frac{\frac{\pi}{2}}{\varphi^1} \right) \right) \quad \textbf{(B3)}$$

where τ_{max} is the mode II interface strength, φ^1 is a CZM mode mixity parameter, and we define κ_1 as:

$$\kappa_1 = \frac{\tau_{max} - \sigma_{max}}{1 - \exp\left(-\frac{\frac{\pi}{2}}{\varphi^1} \right)} \quad \textbf{(B4)}$$

where σ_{max} is the mode I interface strength. In order to obtain an expression for δ_m^* we use the relation of $G = \int_0^\infty T_m(\Delta_n, \Delta_t) d\Delta_m$ which is expanded as

$$G_m = \frac{1}{2} K_m \delta_m^{el\,2} + \int_{\delta_m^{el}}^{\infty} K_m \delta_m^{el} \exp\left(-\frac{\Delta_m^{max} - \delta_m^{el}}{\delta_m^*}\right) d\Delta_m \tag{B5}$$

Rearranging (**B5)** and solving the integral we arrive at our expression for δ_m^*. It is given as follows:

$$\delta_m^* = \frac{G_m}{K_m \delta_m^{el}} - \frac{\delta_m^{el}}{2} \tag{B6}$$

We define G_m as a function of mode angle (φ_{MA}) through the following expression

$$G_m(\varphi_{MA}) = G_t^0 - \kappa_0 \left(1 - \exp\left(-\frac{\frac{\pi}{2}}{\varphi^0}\right)\right) \tag{B7}$$

where G_t^0 is the mode II fracture energy, and where we define κ_0 as

$$\kappa_0 = \frac{G_t^0 - G_n^0}{1 - \exp\left(-\frac{\frac{\pi}{2}}{\varphi^0}\right)} \tag{B8}$$

where G_n^0 is the mode I fracture energy. Finally, we decompose the magnitude of the traction T_m into the normal and tangential components through

$$T_n = \begin{cases} K_{n_{oc}} \Delta_n, \Delta_n < 0 \\ T_m \sin(\varphi_{MA}), \Delta_n \geq 0 \end{cases} \tag{B9}$$

$$T_t = T_m \cos(\varphi_{MA}) \tag{B10}$$

where $K_{n_{oc}}$ is the overclosure penalty stiffness.

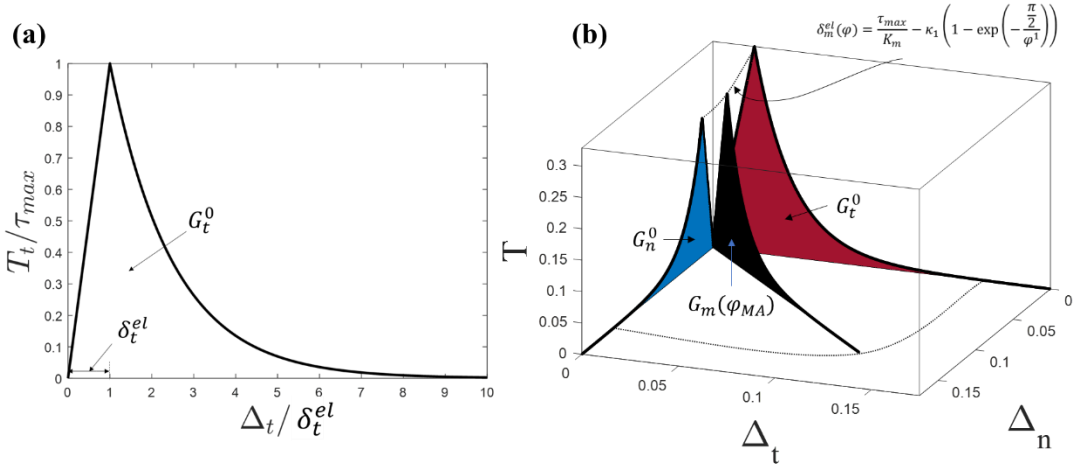

Figure B1. (a) Traction-separation response of the CZM to a mode II separation, δ_t^{el} is the maximum mode II separation allowable

prior to onset of damage, G_t^0 is the area under the traction separation curve; (b) Illustration of the cohesive zone model mixed mode response. Mixed mode response of fracture energy (G), and critical interface strengths (τ, σ), and intrinsic elastic energy $\left(1/2\, K_m \delta_m^{el^2}\right)$ is portrayed.

This formulation represents a significant improvement on previous cohesive zone models in which intrinsic stiffness is dependent on specified fracture energy [36]. Additionally, the requirement of positive instantaneous incremental dissipation [18] is satisfied for all proportional and non-proportional loading paths.

Appendix C: Circumferential Notch Tests

Circumferential notch tests (n=8) were also performed. Notches ($\approx 2.1mm$) were introduced through puncturing the aortic media through the entire specimen width. Notches were then grown manually to ensure a sharp crack tip was present. Notched samples were mounted onto the loading bars as described previously in Figure 4. The extent of the notch was marked with ink prior to testing to allow for accurate measurement of crack growth. Crack growth was also measured after the experiment.

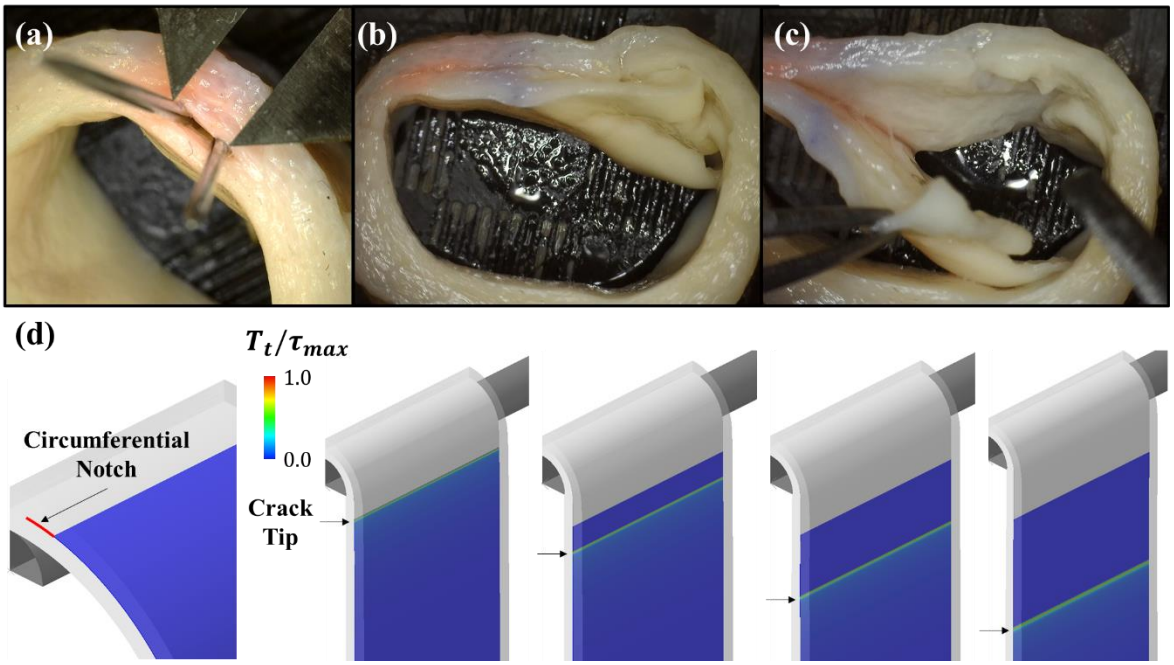

Figure C1. (a) Image of the circumferential notch pre-testing. Circumferential notch is shown measuring approximately ~2 mm; (b) Image of the specimen after testing and prior to ultimate failure. Significant crack growth is observed; (c) Image showing the extent of the circumferential crack growth. Dissected flap is peeled back to reveal the extent of fracture; (d) Finite element simulation of SFRT with a circumferential notch. Extensive crack growth is observed in the *c*-direction in the *c-a* plane. The black arrow indicates the position of the crack tip.

Crack growth was observed in 3 specimens out of the 8 tested. Average crack length was $11.79\text{mm} +/- 4.1\text{mm}$. Aortic dissection is most commonly associated with an intimal tear or notch [33,37–39], however it can and does occur (although less commonly) without a visible entry tear in certain cases [40–43]. This is reflected in the results of our study, all samples tested with a radial notch exhibited extensive mode II crack growth whereas only 3 out of 8 samples with a circumferential notch exhibited mode II crack growth. The mode mixity for the circumferential notch test is also explored in Figure . It shows the same as Figure 4(c) with the addition of the circumferential notch test. The mean mode mixity for the circumferential notch test is $89.18°$.

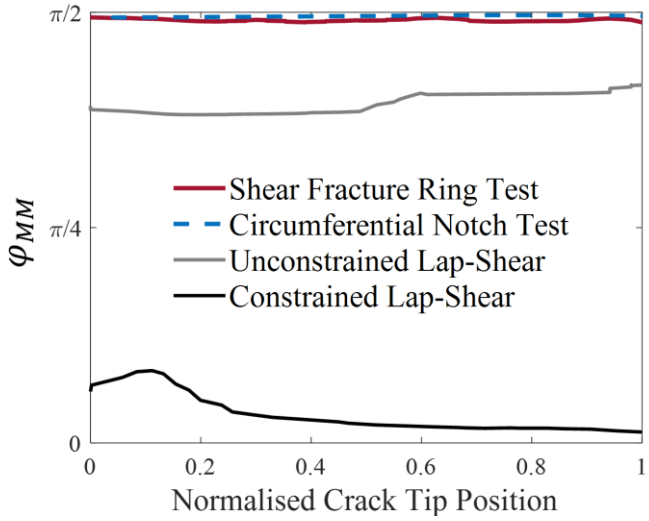

Figure C2. Mode mixity φ_{MM} as a function of normalised crack tip position for the SFRT, circumferential notch test, unconstrained lap-shear, and constrained lap-shear. The mean mode mixity in the circumferential notch test is $89.18°$.

Supplementary Material I: Peel Tests

Methods

To characterise the mode I strength of the tissue, peel tests (n=7) were performed. Tubular sections of aorta were cut along the axial length of the artery resulting in planar sheet specimens. Using a scalpel with a No.10 blade, a notch was introduced at one of the boundary faces [6,9] such that the notch was in the circumferential plane. The notch was then manually grown approximately 2mm to ensure a sharp crack tip. This created two layers (~8-10mm) to be gripped in sandpaper and inserted into the grips of the test machine. Due to the well documented nature of the relatively low levels of anisotropy associated with peel tests and large standard deviation [6,9,44] peel tests (n=7) were conducted in the circumferential direction. The tongues of prepared samples were gripped on either side with sandpaper and placed into the grips of the test machine. A controlled displacement rate of 10.0mm/min was applied to the sample and the resultant reaction force was recorded. The zero level of the force was defined as the force after total separation had occurred.

Results

Experimental curve

Figure shows force/width (mN/mm) as a function of the applied displacement (mm). The mean curve is the thick black curve and each of the individual samples are shown in light grey. The mean force/width is 51.4945 mN/mm, it is shown in dashed red in the figure.

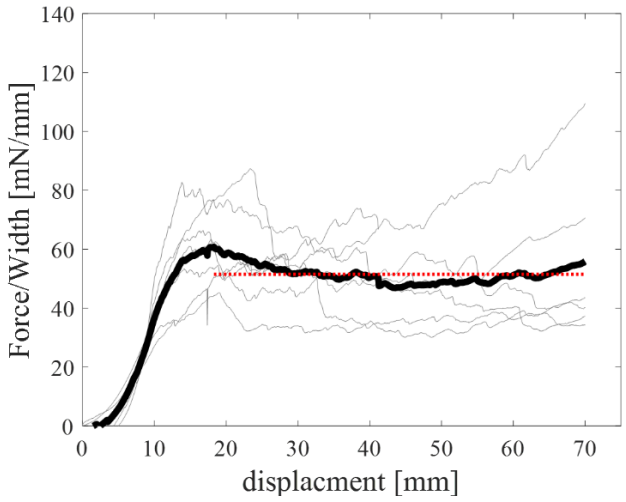

Figure S1a. Force/Width (mN/mm) as a function of the displacement (mm) for the peel test specimens. The mean Force/Width is 51.4945 mN/mm and is denoted by the red dotted line.

Computational fit

All the processes of the experiment are simulated to calibrate our mode I critical interface strength to the peel test data. The sensitivity of the system to variations in the critical interface strength (σ_{max}) and variations in the mode I fracture energy (G_n^0) is investigated in Figure . No sensitivity of the Force/width to the mode II fracture energy (G_n^0) is found. This finding is in agreement with Ferrara and Pandolfi (2010), who found no sensitivity to mode I fracture energy in a numerical study of mode I peel tests of arterial tissue. The sensitivity of the force/width to the critical interface strength is explored in Figure where peel tests of various interface strengths are computed. A median filter is applied to the computed curves to eliminate noise caused by mesh. The mode I critical interface strength of ovine ascending aorta is calculated as $\sigma_{max} = 202kPa$.

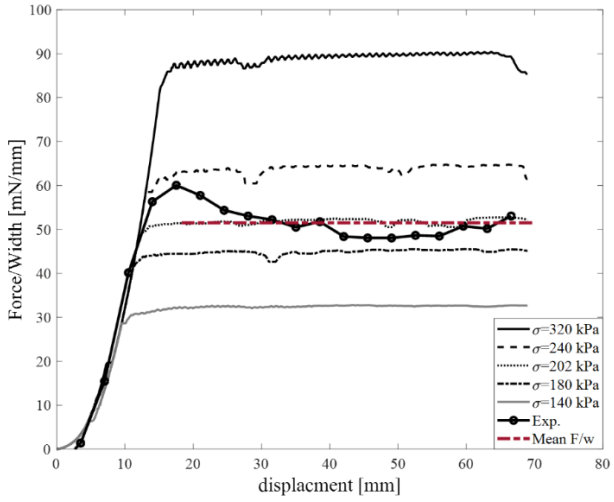

Figure S1b. Computed Force/width curves for several Mode I critical interface strengths. The mean force/width of the ascending ovine aorta undergoing a mode I peel is 51.49 mN/mm

The results of the peel test agree well with published literature. For example, the model presented in the current study with an interface strength of 140kPa calculates a nearly identical mean force/width as seen in previous numerical studies of peel tests (29.03 mN/mm (present study) vs. 28.8 mN/mm [6,7]). The differences in the mean experimental force/width may be partly explained by the difference in species, and anatomical location of the specimens. The mean force/width is in the region of other peel tests carried out on animals (51.49 mN/mm (present study) vs. 67.4 mN/mm [9,16]. Similarly to Ferrara et al. [7], the mode I interface strength is found to be the primary determinant of the mean force/width and no significant influence of the fracture energy is found. Similar behaviour was also observed in the mesh convergence analysis (not here presented) where

higher force/width and oscillations were observed with the coarser mesh and a reduction in force/width and oscillations was observed in the intermediate and finer meshes.

Supplementary Material II: Mesh convergence

In this appendix we present the mesh convergence study carried out on the mesh used to calibrate the mode II interface strength and mode II fracture energy. The circumferential strain at initiation is shown as a function of the number of elements in the mesh. The only model parameter changed in each simulation was the mesh density. Mesh 3 is considered sufficiently accurate and was used for the calibration of the mode II interface strength and the mode II fracture energy.

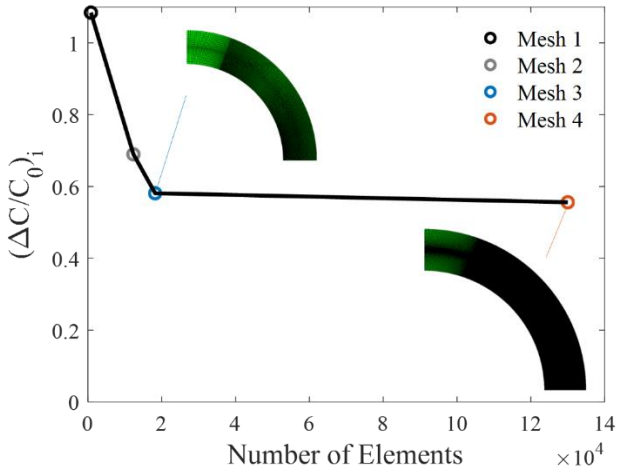

Figure S2. Circumferential strain at initiation as a function of the number of elements in the mesh. Mesh 3 is the converged mesh.

Supplementary Material III: Experimental Images

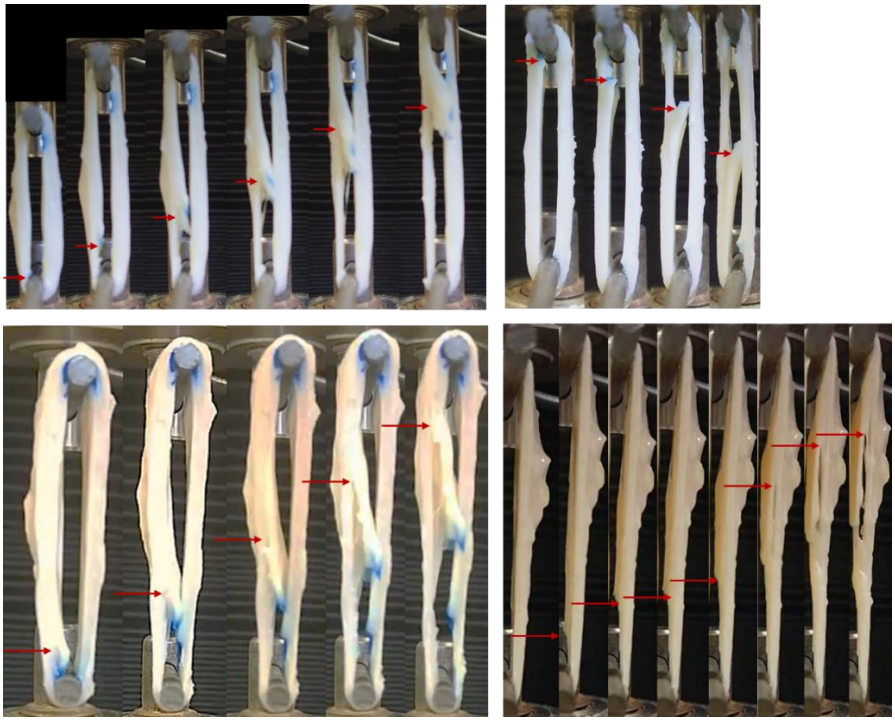

Figure S3: Images of mode II crack propagation in 4 samples undergoing the SFRT. Red arrows approximately indicate the position of the crack tip. Fibrils formed during fibrillation are observed in the top left pane of images.

Acknowledgements: The authors acknowledge funding from grant 16/US-C2C/3291. The authors thank Behrooz Fereidoonezhad, Jamie Concannon, and Lizanne Gallagher for assistance and helpful discussions.

5 References

[1] A. Evangelista, E.M. Isselbacher, E. Bossone, T.G. Gleason, M. Di Eusanio, U. Sechtem, M.P. Ehrlich, S. Trimarchi, A.C. Braverman, T. Myrmel, K.M. Harris, S. Hutchinson, P. O'Gara, T. Suzuki, C.A. Nienaber, K.A. Eagle, Insights from the international registry of acute aortic dissection: A 20-year experience of collaborative clinical research, Circulation. 137 (2018) 1846–1860. https://doi.org/10.1161/CIRCULATIONAHA.117.031264.

[2] F.J. Criado, Aortic dissection: a 250-year perspective., Tex. Heart Inst. J. 38 (2011) 694–700. http://www.pubmedcentral.nih.gov/articlerender.fcgi?artid=3233335&tool=pmcentrez&rendertype=abstract (accessed January 5, 2016).

[3] R. Fattori, P. Cao, P. De Rango, M. Czerny, A. Evangelista, C. Nienaber, H. Rousseau, M. Schepens, Interdisciplinary expert consensus document on management of type B aortic dissection., J. Am. Coll. Cardiol. 61 (2013) 1661–78. https://doi.org/10.1016/j.jacc.2012.11.072.

[4] J. Chikwe, P. Cavallaro, S. Itagaki, M. Seigerman, G. Diluozzo, D.H. Adams, National outcomes in acute aortic dissection: Influence of surgeon and institutional volume on operative mortality, Ann. Thorac. Surg. 95 (2013) 1563–1569. https://doi.org/10.1016/j.athoracsur.2013.02.039.

[5] T.C. Gasser, G.A. Holzapfel, Modeling the propagation of arterial dissection, Eur. J. Mech. - A/Solids. 25 (2006) 617–633. https://doi.org/10.1016/j.euromechsol.2006.05.004.

[6] G. Sommer, T.C. Gasser, P. Regitnig, M. Auer, G.A. Holzapfel, Dissection properties of the human aortic media: an experimental study., J. Biomech. Eng. 130 (2008) 021007. https://doi.org/10.1115/1.2898733.

[7] A. Ferrara, A. Pandolfi, A numerical study of arterial media dissection processes, in: Int. J. Fract., Springer Netherlands, 2010: pp. 21–33. https://doi.org/10.1007/s10704-010-9480-y.

[8] J. Tong, G. Sommer, P. Regitnig, G.A. Holzapfel, Dissection properties and mechanical strength of tissue components in human carotid bifurcations, Ann. Biomed. Eng. 39 (2011) 1703–1719. https://doi.org/10.1007/s10439-011-0264-y.

[9] C. Noble, N. Smulders, R. Lewis, M.J. Carré, S.E. Franklin, S. MacNeil, Z.A. Taylor, Controlled peel testing of a model tissue for diseased aorta, J. Biomech. 49 (2016) 3667–3675. https://doi.org/10.1016/j.jbiomech.2016.09.040.

[10] C. Noble, O. van der Sluis, R.M.J. Voncken, O. Burke, S.E. Franklin, R. Lewis, Z.A. Taylor, Simulation of arterial dissection by a penetrating external body using cohesive zone modelling, J. Mech. Behav. Biomed. Mater. 71 (2017) 95–105. https://doi.org/10.1016/j.jmbbm.2017.03.004.

[11] P.G. Hagan, C.A. Nienaber, E.M. Isselbacher, D. Bruckman, D.J. Karavite, P.L. Russman, A. Evangelista, R. Fattori, toru Suzuki, J.K. Oh, A.G. Moore, J.F. Malouf, L.A. PAPe, C. Gaca, U. Sechtem, S. Lenferink, H.J. Deutsch, H. Diedrichs, J.M. Robles, A. Llovet, D. Gilon, S.K. Das, W.F. Armstrong, G.M. Deeb, K.A. Eagle, The International Registry of Acute Aortic Dissection (IRAD), J. Am. Med. Assoc. 283 (2000) 897–903. https://doi.org/10.1001/jama.283.7.897.

[12] P. Eshtehardi, P. Adorjan, M. Togni, H. Tevaearai, R. Vogel, C. Seiler, B. Meier, S. Windecker, T. Carrel, P. Wenaweser, S. Cook, Iatrogenic left main coronary artery dissection: Incidence, classification, management, and long-term follow-up, Am. Heart J. 159 (2010) 1147–1153. https://doi.org/10.1016/j.ahj.2010.03.012.

[13] S. Trimarchi, T. Tsai, K.A. Eagle, E.M. Isselbacher, J. Froehlich, J. V. Cooper, V. Rampoldi, G.R. Upchurch, Acute abdominal aortic dissection: Insight from the International Registry of Acute Aortic Dissection (IRAD), J. Vasc. Surg. 46 (2007) 913-919.e1. https://doi.org/10.1016/J.JVS.2007.07.030.

[14] H.W. Haslach, A. Siddiqui, A. Weerasooriya, R. Nguyen, J. Roshgadol, N. Monforte, E. McMahon, Fracture mechanics of shear crack propagation and dissection in the healthy bovine descending aortic media, Acta Biomater. 68 (2018) 53–66. https://doi.org/10.1016/j.actbio.2017.12.027.

[15] C. van Baardwijk, M.R. Roach, Factors in the propagation of aortic dissections in canine thoracic aortas, J. Biomech. 20 (1987) 67–73. https://doi.org/10.1016/0021-9290(87)90268-5.

[16] C.M. Witzenburg, R.Y. Dhume, S.B. Shah, C.E. Korenczuk, H.P. Wagner, P.W. Alford, V.H. Barocas, Failure of the porcine ascending aorta: Multidirectional experiments and a unifying microstructural model, J. Biomech. Eng. 139 (2017). https://doi.org/10.1115/1.4035264.

[17] G. Sommer, S. Sherifova, P.J. Oberwalder, O.E. Dapunt, P.A. Ursomanno, A. DeAnda, B.E. Griffith, G.A. Holzapfel, Mechanical strength of aneurysmatic and dissected human thoracic aortas at different shear loading modes, J. Biomech. 49 (2016) 2374–2382. https://doi.org/10.1016/j.jbiomech.2016.02.042.

[18] J.P. McGarry, É. Ó Máirtín, G. Parry, G.E. Beltz, Potential-based and non-potential-based cohesive zone formulations under mixed-mode separation and over-closure. Part I: Theoretical analysis, J. Mech. Phys. Solids. 63 (2014) 336–362. https://doi.org/10.1016/j.jmps.2013.08.020.

[19] G. Parry, P. McGarry, An analytical solution for the stress state at stent-coating interfaces, J. Mech. Behav. Biomed. Mater. 10 (2012) 183–196. https://doi.org/10.1016/j.jmbbm.2012.02.009.

[20] D.R. Nolan, A.L. Gower, M. Destrade, R.W. Ogden, J.P. McGarry, A robust anisotropic hyperelastic formulation for the modelling of soft tissue, J. Mech. Behav. Biomed. Mater. 39 (2014) 48–60. https://doi.org/10.1016/j.jmbbm.2014.06.016.

[21] T.C. Gasser, R.W. Ogden, G.A. Holzapfel, Hyperelastic modelling of arterial layers with distributed collagen fibre orientations., J. R. Soc. Interface. 3 (2006) 15–35. https://doi.org/10.1098/rsif.2005.0073.

[22] D.R. Nolan, J.P. McGarry, On the correct interpretation of measured force and calculation of material stress in biaxial tests, J. Mech. Behav. Biomed. Mater. 53 (2016) 187–199. https://doi.org/10.1016/j.jmbbm.2015.08.019.

[23] D.C. Miller, R.S. Mitchell, P.E. Oyer, E.B. Stinson, S.W. Jamieson, N.E. Shumway, Independent determinants of operative mortality for patients with aortic dissections., Circulation. 70 (1984) I153-64. http://europepmc.org/abstract/med/6235061 (accessed January 4, 2016).

[24] A. Tsamis, J.T. Krawiec, D.A. Vorp, Elastin and collagen fibre microstructure of the human aorta in ageing and disease: a review., J. R. Soc. Interface. 10 (2013) 20121004. https://doi.org/10.1098/rsif.2012.1004.

[25] H. Sariola, T. Viljanen, R. Luosto, Histological pattern and changes in extracellular matrix in aortic dissections, J. Clin. Pathol. 39 (1986) 1074–1081. https://doi.org/10.1136/jcp.39.10.1074.

[26] S.A. Lemaire, L. Russell, Epidemiology of thoracic aortic dissection, Nat. Rev. Cardiol. 8 (2011) 103–113. https://doi.org/10.1038/nrcardio.2010.187.

[27] Y. Nakashima, Y. Shiokawa, K. Sueishi, Alterations of elastic architecture in human aortic dissecting aneurysm., Lab. Invest. 62 (1990) 751–60. http://www.ncbi.nlm.nih.gov/pubmed/2359259 (accessed February 2, 2018).

[28] P.A. Abraham, A.J. Perejda, W.H. Carnes, J. Uitto, Marfan syndrome. Demonstration of abnormal elastin in aorta, J. Clin. Invest. 70 (1982) 1245–1252. https://doi.org/10.1172/JCI110723.

[29] S.-M. Yuan, H. Jing, Cystic medial necrosis: pathological findings and clinical implications, Rev. Bras. Cir. Cardiovasc. 26 (2011) 107–115. https://doi.org/10.1590/S0102-76382011000100019.

[30] T. Brandt, E. Orberk, R. Weber, I. Werner, O. Busse, B.T. Müller, F. Wigger, A. Grau, C. Grond-Ginsbach, I. Hausser, Pathogenesis of cervical artery dissections: Association with connective tissue abnormalities, Neurology. 57 (2001) 24–30. https://doi.org/10.1212/WNL.57.1.24.

[31] D. Ulbricht, N.J. Diederich, T. Hermanns-Lê, R.J. Metz, F. Macian, G.E. Piérard, Cervical artery dissection: An atypical presentation with Ehlers-Danlos-like collagen pathology?, Neurology. 63 (2004) 1708–1710. https://doi.org/10.1212/01.WNL.0000142970.09454.30.

[32] T.L. Anderson, Fracture Mechanics, CRC Press, 2005. https://doi.org/10.1201/9781420058215.

[33] E.W. Larson, W.D. Edwards, Risk factors for aortic dissection: A necropsy study of 161 cases, Am. J. Cardiol. 53 (1984) 849–855. https://doi.org/10.1016/0002-9149(84)90418-1.

[34] M.D. Dake, M. Thompson, M. van Sambeek, F. Vermassen, J.P. Morales, DISSECT: a new mnemonic-based approach to the categorization of aortic dissection., Eur. J. Vasc. Endovasc. Surg. 46 (2013) 175–90. https://doi.org/10.1016/j.ejvs.2013.04.029.

[35] D.R. Nolan, J.P. McGarry, On the Compressibility of Arterial Tissue, Ann. Biomed. Eng. 44 (2016) 993–1007. https://doi.org/10.1007/s10439-015-1417-1.

[36] J.P. McGarry, P.E. McHugh, Modelling of in vitro chondrocyte detachment, J. Mech. Phys. Solids. 56 (2008) 1554–1565. https://doi.org/10.1016/j.jmps.2007.08.001.

[37] R.E. Clough, C.A. Nienaber, Management of acute aortic syndrome., Nat. Rev. Cardiol. 12 (2015) 103–14. https://doi.org/10.1038/nrcardio.2014.203.

[38] A. Karthikesalingam, P.J.E. Holt, R.J. Hinchliffe, M.M. Thompson, I.M. Loftus, The diagnosis and management of aortic dissection., Vasc. Endovascular Surg. 44 (2010) 165–9. https://doi.org/10.1177/1538574410362118.

[39] R. Aun, Acute aortic dissection, in: Endovasc. Hybrid Ther. Struct. Hear. Aortic Dis., Elsevier, 2013: pp. 74–89. https://doi.org/10.1002/9781118504536.ch8.

[40] A. Colli, M. Carrozzini, A. Francescato, M. Galuppo, M. Comisso, F. Toto, D. Gregori, G. Gerosa, Acute DeBakey Type I aortic dissection without intimal tear in the arch: is total arch replacement the right choice?, Interact. Cardiovasc. Thorac. Surg. 26 (2018) 84–90. https://doi.org/10.1093/icvts/ivx229.

[41] R.C. Lui, A.H. Menkis, F.N. McKenzie, Aortic dissection without intimal rupture: Diagnosis and management, Ann. Thorac. Surg. 53 (1992) 886–888. https://doi.org/10.1016/0003-4975(92)91460-Q.

[42] A.E. Hirst, V.J. Johns, S.W. Kime, Dissecting aneurysm of the aorta: A review of 505 cases, Med. (United States). 37 (1958) 217–279. https://doi.org/10.1097/00005792-195809000-00003.

[43] S.K. Wilson, G.M. Hutchins, Aortic dissecting aneurysms. Causative factors in 204 subjects, Arch. Pathol. Lab. Med. 106 (1982) 175–180. http://www.ncbi.nlm.nih.gov/pubmed/6895989 (accessed January 18, 2020).

[44] J. Tong, G. Sommer, P. Regitnig, G.A. Holzapfel, Dissection Properties and Mechanical Strength of Tissue Components in Human Carotid Bifurcations, Ann. Biomed. Eng. 39 (2011) 1703–1719. https://doi.org/10.1007/s10439-011-0264-y.